Modeling the Climatology of Low- and Mid-Latitude F-Region Ionospheric Currents Using the Swarm Constellation

M. Fillion[1,2,3], G. Hulot[3] , P. Alken[1,2] , and A. Chulliat[1,2]

[1]Cooperative Institute for Research in Environmental Sciences, University of Colorado, Boulder, CO, USA, [2]NOAA National Centers for Environmental Information, Boulder, CO, USA, [3]Université Paris Cité, Institut de physique du globe de Paris, CNRS, Paris, France

Abstract We present a new empirical model of quiet-time F-region ionospheric currents and associated magnetic fields. This model is designed to accurately represent these currents and fields at low and mid latitudes. For each individual Swarm satellite, the preprocessed data is represented as a non-potential toroidal magnetic field using the Mie representation in a thin-shell and spherical harmonic expansions. This approach allows to fully separate spatial and climatological variations as well as to assess the robustness of the model with respect to both measurement errors and data sampling with local time. The obtained model describes the toroidal magnetic fields and the associated radial poloidal electric currents at two distinct altitudes in the ionosphere F region. Clear signatures of low- and mid-latitude interhemispheric field-aligned currents (IHFACs) are identified. The model reproduces well-known characteristics of the climatology of IHFACs and provides new insights, for example, on the average daily variations of IHFACs during winter in the Northern Hemisphere. It also well recovers the variations of IHFACs with longitude. The potential driving mechanisms of these variations, such as longitudinal variations of the main field and modulation by upward propagating atmospheric tides, are discussed. The new model can be used to analyze the relationship between atmospheric tides and IHFACs. It can also be used to investigate the connection between the magnetic fields and electric currents from the ionospheric E and F regions in order to improve the separation of these fields as well as our understanding of the overall ionospheric electric current system.

1. Introduction

The Earth's magnetic field is the sum of magnetic fields produced by many different sources. It can be measured at the Earth's surface, in the geomagnetic observatories, or on board of satellites (Hulot et al., 2015). Such data are used to build models of the Earth's magnetic field and to study their sources. One main challenge, however, is to single out the signal from each source. This is particularly true for the ionospheric field produced by the electric currents that flow in the ionosphere—the ionized layer of the atmosphere, from 80 to 1,000 km. Because of its high variability in space and time, and of an incomplete space-time data coverage, this field and associated electric currents are still only partially understood (Finlay et al., 2017).

One of the dominant ionospheric currents at mid and low latitudes are called *Solar quiet* (*Sq*) currents (Matsushita, 1968; Yamazaki & Maute, 2017). They flow in the ionospheric E region—between 90 and 150 km—and mainly consist of two vortices, each flowing in one hemisphere and in opposite directions. They are generated by a physical mechanism called the *ionospheric wind dynamo* (Richmond, 1979) and are therefore referred to as dynamo currents. This system is reinforced at the magnetic equator where the equatorial electrojet flows (Lühr et al., 2021). Several approaches have been proposed to build data-based models of the mid- and low-latitude E-region ionospheric field. The Comprehensive Model series (Sabaka et al., 2002, 2020) and the DIFI model (Chulliat et al., 2013, 2016) use spherical harmonics and Fourier series to represent the global climatological variations of the low and mid latitude E-region ionospheric field. More recently, some alternative approaches were developed. They rely on a priori information allowing for a better characterization of individual Earth's magnetic field component. Among these, one can mention correlation-based modeling techniques (Baerenzung et al., 2020; Holschneider et al., 2016) and techniques that rely on physics-based models (Alken et al., 2017; Egbert et al., 2021).

Other important ionospheric currents flow in the F region, between 150 and 1,000 km. These currents are of particular interest to this study. The dominant currents in the F region are the field-aligned currents that flow along the highly conductive field lines of the Earth's main magnetic field. They exist both at high latitudes

and low and mid latitudes and are produced by distinct physical mechanisms in these two latitude sectors. In the mid- and low-latitude F region, interhemispheric field-aligned currents (IHFACs) arise from the electrostatic difference between geomagnetic conjugate points and connect the E-region dynamo current systems in the Northern and Southern Hemispheres (Fukushima, 1978; Takeda, 1982; Van Sabben, 1966). These currents mostly flow on the dayside and have been extensively studied using ground and satellite data (Bolaji et al., 2012; Fillion et al., 2021; Lühr et al., 2015, 2019; Park et al., 2011; Park, Stolle, et al., 2020; Park, Yamazaki, & Lühr, 2020; Ranasinghe et al., 2021; Shinbori et al., 2017; Yamashita, 2002). At high latitudes, field-aligned currents are about one order of magnitude more intense and connect the high-latitude E-region current system to magnetospheric currents. They flow at all local times and are organized in two cells respectively in the dawn and dusk sectors (Laundal et al., 2016; Weimer et al., 2010). Additionally, significant dynamo currents also flow in the mid- and low-latitude ionospheric F-region (Maute & Richmond, 2017; Rishbeth, 1981, 1997; Van Sabben, 1966). Some of the best documented dynamo currents in this region are the meridional dynamo currents first introduced by Rishbeth (1971), which flow above the magnetic equator (Lühr & Maus, 2006; Lühr et al., 2019; Park et al., 2010; H. Wang, Lühr, et al., 2022). A complete review of F region dynamo currents can be found in Maute and Richmond (2017).

Olsen (1997) produced one of the first data-based F-region models. This study proposed two methods to recover the F region toroidal magnetic and associated poloidal current using data from the Magsat satellite. He was able to identify high-latitude ionospheric field-aligned currents, meridional dynamo currents as well as mid-latitude field-aligned currents. His model, however, was limited to two local times due to the local time coverage of the Magsat mission. F-region currents and magnetic fields were also included in pre-Swarm versions of the Comprehensive Model (Sabaka et al., 2002, 2015). This model was also able to predict some features of F-region field-aligned and meridional dynamo currents. The most recent versions, however, no longer include F-region currents (Sabaka et al., 2018, 2020). More recently, Laundal et al. (2018) developed the AMPS model which is specifically designed to represent the E- and F-region currents and magnetic fields at high latitudes. Some studies have also used the Spherical Elementary Current Systems techniques that can be applied at both global or local scales (Amm et al., 2015; Amm & Viljanen, 1999).

The Swarm constellation, launched in 2013, now provides a dataset with unprecedented spatial and temporal coverage (Friis-Christensen et al., 2006; Olsen et al., 2013). While recent models such as AMPS represent the high-latitude F-region currents and fields, to the authors' knowledge, no recent model takes full advantage of the Swarm constellation to represent the global mid- and low-latitude F-region currents and fields. In this study, we present the first step toward building such a model. This kind of model will improve our understanding of the ionospheric electric current system, which would in turns improve our ability to model the geomagnetic field as well as our understanding of ionospheric physics. One difficulty, however, is that satellite measures a time-varying magnetic field while moving through space, thus mixing spatial and temporal signals in the measurements. In this study, our goal is to investigate whether a full separation of spatial and climatological variations can be achieved using the Swarm data. We show that our preliminary model can recover well-known characteristics of F region currents and can provide new insights. Section 2 details the data used in this work and the preprocessing and selection. Sections 3 and 4 present the model parametrization and the inversion procedure. In Section 5, we then discuss the model fit to the data and in Section 6.1 we validate the model by comparing current density maps to results obtained in previous studies. In Sections 6.2 and 6.3, the model is used to investigate the climatology of F-region currents. Section 7 concludes this paper.

2. Data Selection and Pre-Processing

The Swarm satellite constellation consists of three identical satellites, launched into near-polar orbits on 22 November 2013 (Friis-Christensen et al., 2006). The satellites, respectively known as Alpha, Bravo and Charlie, reached their configuration for the period ranging from 2014 to 2022 in May 2014; Alpha and Charlie were lowered to an average altitude of 460 km and flew on close by orbits whereas Bravo was raised to an average altitude of 530 km. For each satellite, the local time at the ascending node (resp. descending node) slowly drifts such that one satellite covers all local time sectors in about 4 months. The drift rates are also different for Swarm Bravo on one side and Swarm Alpha and Charlie on the other, meaning that the satellites gradually separate in local time. All satellites carry an Absolute Scalar Magnetometer (ASM) (Léger et al., 2015) and a Vector Fluxgate Magnetometer (VFM) (Merayo et al., 2008) measuring the intensity and the direction of the geomagnetic field, respectively.

We use Level-1b 1 Hz vector data from the Swarm data processing chain (Olsen et al., 2013) version 0601. The data are first corrected for several potential fields: the core field, the lithospheric field, the ionospheric E-region field and its induced counterpart, and the magnetospheric field and its induced counterpart using the Swarm-derived Comprehensive Model (CM) (Sabaka et al., 2018) version 0701. The use of the comprehensive model is mainly motivated by two considerations. First, this model is built using a comprehensive approach specifically designed to optimize field separation (Sabaka & Olsen, 2006). Second, the representation of the magnetospheric field in the CM is based on static low-degree spherical harmonics representations in 1-hr bins. This approach fairly accounts for the fast-varying quiet-time magnetospheric field which turned out to be critical to limit contamination and extract meaningful F-region currents. The data are then decimated every 60s and selected for quiet time by only retaining data when the *ap* index was below 10 (Matzka et al., 2021).

A good data coverage is critical to accurately recover the average climatological variations of the F-region toroidal field and associated currents. We therefore use data from 1 January 2016 to 31 December 2020 from all three Swarm satellites. This dataset ensures that all longitude sectors are well covered for every local time and every season. This is illustrated in Figure 1 for Swarm satellites Alpha and Bravo. This figure presents histograms of the number of data in every local time and longitude sectors for each season and for satellites Alpha and Bravo after the above-mentioned data selection and decimation—note that the local time coverage of Swarm Charlie is the same as Swarm Alpha for the considered period of time—. Each season is defined as a 91 day period either centered on the solstice or the equinox. The data coverage is generally slightly better during Northern Hemisphere summer, although overall it is good for all seasons. Additionally, the start and end dates were chosen to keep only a period of time during which satellite Bravo was separated from satellites Alpha and Charlie by at least 1 hour in local time. This ensures that Swarm Bravo sampled the local time sectors completely independently of Swarm Alpha and Charlie, that is the three satellites never measured the magnetic field in the same local time sector simultaneously. Furthermore, it also corresponds to a period of time when the daily average distance from the Earth's center for each satellite did not vary by more than 20 km. This is an important consideration with respect to the parametrization presented in Section 3. Finally, for the sake of simplicity, any reference to a specific season in the following will refer to the corresponding season in the Northern Hemisphere.

3. Parametrization

The parametrization relies on an approximation of the Mie representation of the magnetic field in a thin spherical shell. This approximation is called the thin-shell approximation (Backus, 1986; Sabaka et al., 2010). Using this mathematical representation, the magnetic field within a thin spherical shell of minimum radius a, maximum radius c and thickness $c - a = h$ can be expressed as the sum of three terms:

$$\vec{B}(r, \theta, \phi, t) = \vec{B}_i(r, \theta, \phi, t) + \vec{B}_e(r, \theta, \phi, t) + \vec{B}_T(b, \theta, \phi, t) \tag{1}$$

where r, θ, ϕ and t are respectively the radius, colatitude, longitude and time, with r varying between a and c, $\vec{B}_i$ is the internal poloidal magnetic field produced by sources located inside the sphere of radius a, $\vec{B}_e$ the external poloidal magnetic field produced by the sources located outside the sphere of radius c, and $\vec{B}_T$ the toroidal magnetic field on the average sphere of the shell with radius $b = \frac{c+a}{2}$ produced by electric currents crossing this sphere. Note that, in Equation 1, two contributions to the total magnetic field are neglected. The first is associated with the radial variations of the toroidal field $\vec{B}_T$ within the shell. The second is associated with the poloidal magnetic field produced by the currents that flow within the shell (between the spheres of radius a and c). Both contributions are of the order of $\frac{h}{b}$ and are small enough to be neglected (Sabaka et al., 2010).

The thin-shell approximation is very well suited to model the magnetic field measured by the Swarm satellites. Indeed, each Swarm satellite orbit inside a thin spherical shell whose minimum and maximum radius are defined by the minimum and maximum radius reached by the satellite during the considered period of time. Figure 2 shows the overall configuration. The spherical shell corresponding to Swarm Alpha and Charlie is represented in blue and the shell corresponding to Swarm Bravo in red. The low- and mid-latitude IHFACs and the E-region Sq dynamo currents are also represented. Between 1 January 2016 and 31 December 2020, the minimum and maximum radius are $a_{AC} \approx 432$ km and $c_{AC} \approx 483$ km for Swarm satellites Alpha and Charlie, and $a_B \approx 498$ km and $c_B \approx 532$ km for Swarm satellite Bravo. The corresponding shell thicknesses are $h_{AC} \approx 51$ km and $h_B \approx 34$ km. Note also that, since $c_{AC} < a_B$, Swarm Alpha/Charlie and Swarm Bravo measure the magnetic field within non-intersecting shells.
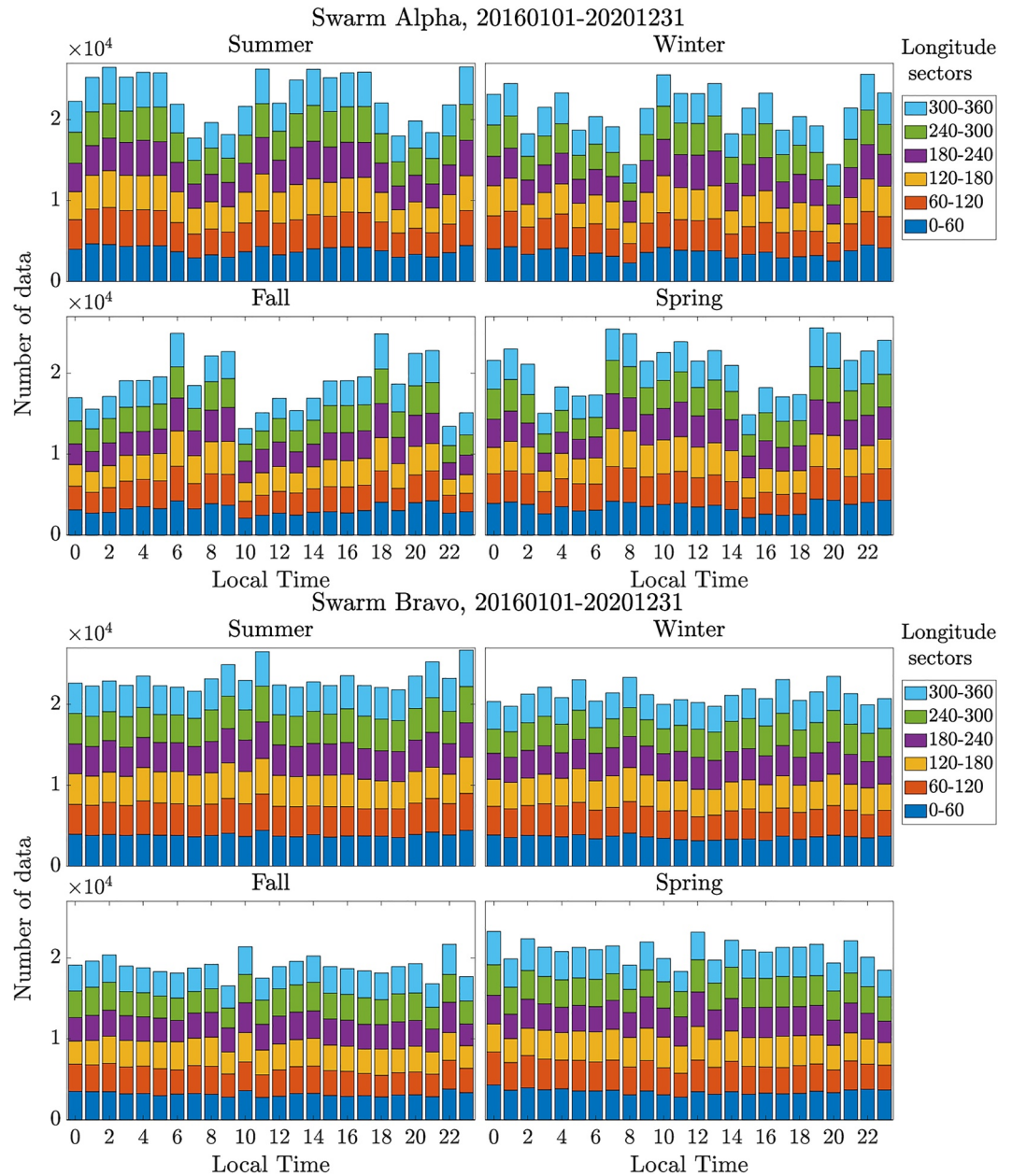
Figure 1. Histograms showing the data coverage for Swarm Alpha (top four panels) and Swarm Bravo (bottom four panels) between 1 January 2016 and 31 December 2020 after data selection and decimation. Each panel shows the data distribution in one-hour local time sectors for a specific season. Additionally, information about the longitudinal distribution for each local time sector is given using the color code detailed in the legends.

We use Equation 1 to express the magnetic field measured by each Swarm satellite. We also assume that subtracting the magnetic field prediction of the Comprehensive Model from the data (Section 2) correctly removes all contributions from the poloidal fields—the first two terms on the right side of Equation 1. The Comprehensive Model, however, like other similar models, cannot exactly capture all of the poloidal fields and we note that possible contamination of the model by residual potential fields must be considered when interpreting our model. Neglecting $\vec{B}_i$ and $\vec{B}_e$ in Equation 1 then leads to:

$$\vec{B}(r,\theta,\phi,t) = \vec{B}_T(b,\theta,\phi,t) \tag{2}$$

Equation 2 is a compact representation of three independent equations, one equation for each Swarm satellite. Note that, in this equation, $\vec{B}$ does not vary as a function of the spherical coordinate r inside the considered thin
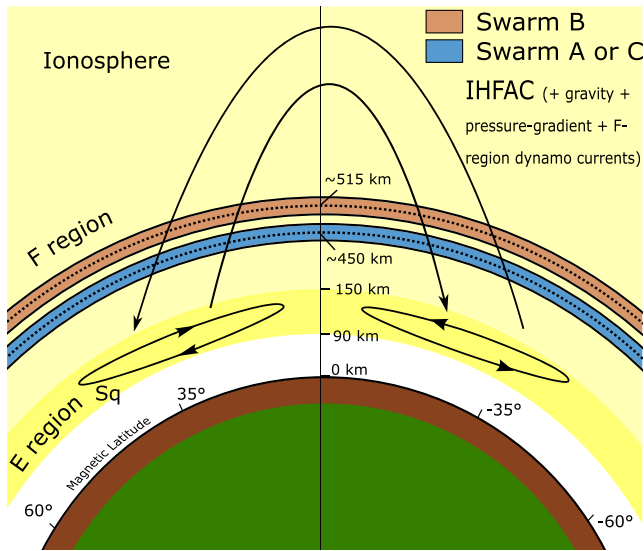
Figure 2. Sketch of the overall configuration. Swarm Bravo orbits within the red spherical shell whereas Swarm Alpha and Charlie orbit within the blue one. The low and mid-latitude IHFACs and the E-region Sq dynamo currents are represented with black arrows.

spherical shell. The toroidal magnetic field can be further expressed using the toroidal potential Φ, which gives:

$$\vec{B}_T(r,\theta,\phi,t) = \vec{\nabla} \times \left(\Phi(b,\theta,\phi,t)\vec{r} \right) \tag{3}$$

where $\vec{\nabla}\times$ is the curl operator and $\vec{r}$ is the position vector where the field is to be evaluated. Equation 3 shows that the toroidal field $\vec{B}_T$ has no radial component. The two other components can be calculated using the following equations:

$$B_\theta(r,\theta,\phi,t) = \frac{1}{\sin\theta}\frac{\partial}{\partial\phi}\Phi(b,\theta,\phi,t) \tag{4}$$

$$B_\phi(r,\theta,\phi,t) = -\frac{\partial}{\partial\theta}\Phi(b,\theta,\phi,t) \tag{5}$$

where B_θ and B_ϕ are respectively the South and East components. Additionally, the three components of the poloidal current at the position $\vec{r}$ and time t can also be derived from the toroidal potential Φ using the following equations:

$$J_r(r,\theta,\phi,t) = \frac{-1}{\mu_0 r}\nabla_S^2(\Phi(b,\theta,\phi,t)) \tag{6}$$

$$J_\theta(r,\theta,\phi,t) = \frac{1}{\mu_0 r}\frac{\partial}{\partial\theta}\frac{\partial}{\partial r}(r\Phi(b,\theta,\phi,t)) \tag{7}$$

$$J_\phi(r,\theta,\phi,t) = \frac{1}{\mu_0 r\sin\theta}\frac{\partial}{\partial\phi}\frac{\partial}{\partial r}(r\Phi(b,\theta,\phi,t)) \tag{8}$$

where J_r, J_θ and J_ϕ are respectively the Radial, South and East components and ∇_S^2 is the surface Laplacian defined as:

$$\nabla_S^2 = \frac{1}{\sin\theta}\frac{\partial}{\partial\theta}\left(\sin\theta\frac{\partial}{\partial\theta}\right) + \frac{1}{\sin^2\theta}\frac{\partial^2}{\partial\phi^2} \tag{9}$$

The next step is to express Φ with a parametrized equation. We choose to represent the spatial variations of Φ with a truncated spherical harmonics expansion and adopt the same approach as the one used in former versions of the comprehensive model (Sabaka et al., 2002, 2015). This approach relies on a modulation of the spatial part with harmonic functions of time. This is also the approach used to model the E-region ionospheric field in the Comprehensive Model (Sabaka et al., 2020) and DIFI model (Chulliat et al., 2013, 2016). The full expression of the toroidal potential Φ is the following:

$$
\begin{aligned}
\Phi(r,\theta,\phi,t,t_{UT}) = &\sum_{s=s_{\min}}^{s_{\max}}\sum_{p=p_{\min}}^{p_{\max}}\sum_{n=1}^{n_{\max}}\sum_{m=0}^{\min(n,m_{\max})} P_n^m(\cos\theta)\\
&\left\{\left[\varphi_{nsp}^{m,(c)}\cos(m\phi) + \psi_{nsp}^{m,(c)}\sin(m\phi)\right]\cos(\omega_s st + \omega_p pt_{UT})\right.\\
&\left.+ \left[\varphi_{nsp}^{m,(s)}\cos(m\phi) + \psi_{nsp}^{m,(s)}\sin(m\phi)\right]\sin(\omega_s st + \omega_p pt_{UT})\right\}
\end{aligned} \tag{10}
$$

where t and t_{UT} are the time respectively expressed in decimal years between 0 and 1 and in hours between 0 and 24, n and m are the degree and the order of the spherical harmonics expansion, s and p are the wave numbers respectively associated with seasonal and diurnal modes, P_n^m are the Schmidt Seminormalized Associated Legendre functions (Winch et al., 2005), ω_s is the seasonal angular frequency equal to 2π rad.yr^{-1}, ω_p is the diurnal angular fundamental frequency equal to $\frac{2\pi}{24}$ rad.hr^{-1}, and $\varphi_{nsp}^{m,(c)}$, $\psi_{nsp}^{m,(c)}$, $\varphi_{nsp}^{m,(s)}$ and $\psi_{nsp}^{m,(s)}$ are the model coefficients. We obtain a set of three identical equations for Φ_A, Φ_B, and Φ_C with a different set of coefficients for each equation. Note that we do not use magnetic coordinates—such as the quasi dipole coordinates (Richmond, 1995)—or magnetic time, but the standard spherical coordinates and UTC time. This is done on purpose and will allow us to check if the recovered signal is naturally organized with respect to the Earth's main magnetic field, as we expect, despite the fact that this is not constrained by the parametrization.

We choose $n_{\max} = 60$ and $m_{\max} = 10$. The truncation degree is taken relatively high in order to correctly capture the sharp transition between the mid- and high-latitude current systems. In contrast, the maximum order is set relatively low. This is to limit contamination by the meridionally organized fast-varying magnetospheric field. Finally, following Chulliat et al. (2016) and Sabaka et al. (2020), we set $s_{\min} = -2$, $s_{\max} = 2$, $p_{\min} = 0$, and $p_{\max} = 4$. It respectively corresponds to the 24, 12, 8, and 6-hr diurnal modes as well as the semiannual and annual modes. This results in a total number of 57,330 coefficients. Assuming that one knows the model coefficients, one can directly compute B_θ, B_ϕ, and J_r on the sphere of radius b by inserting Equation 10 in Equations 4–6. However, according to Equations 7 and 8, computing J_θ and J_ϕ is not possible as additional knowledge of the radial derivatives of the model coefficients would then be required.

4. Inversion Procedure

We derive three independent spherical harmonics representations using the parametrization presented in Section 3 and the same inversion procedure. Each representation is computed using data from one Swarm satellite. Model A, B, and C will respectively refer to the representation derived with data from Swarm Alpha, Bravo, and Charlie. The forward problems can be written as:

$$\vec{d} = \boldsymbol{G}\vec{m} \tag{11}$$

where $\vec{d}$ is the data vector, which only includes the South and East components of the satellite measurements, $\vec{m}$ is the model vector which contains the model coefficients and $\boldsymbol{G}$ is the matrix that connects the two vectors. We compute estimates of the parameter vectors by minimizing the following cost functions:

$$\vec{e}^T \boldsymbol{C}_d^{-1} \vec{e} + \lambda \vec{m}^T \boldsymbol{\Lambda} \vec{m} \tag{12}$$

where $\vec{e}$ is the residual vector, $\boldsymbol{C}_d$ is the a priori diagonal data covariance matrix for which we take all elements equal to 1 nT^{-2}, the matrix $\boldsymbol{\Lambda}$ is a regularization matrix, the coefficient λ is a damping parameter and T denotes the matrix transpose. $\boldsymbol{\Lambda}$ is a diagonal matrix which is defined as:

$$\boldsymbol{\Lambda} = \boldsymbol{I}_{(49)} \otimes \boldsymbol{\Omega} \tag{13}$$

where $\boldsymbol{I}_{(49)}$ is the identity matrix of dimension 49×49, 49 corresponding to the total number of temporal basis functions, $\boldsymbol{\Omega}$ is a diagonal matrix of dimension 1,170×1,170, 1,170 corresponding to the total number of spatial basis functions, and $\otimes$ is the Kronecker product as defined by Loan (2000). The elements of the matrix $\boldsymbol{\Omega}$ are defined as:

$$\Omega_{nm,n'm'} = \frac{1}{2} \frac{n^4(n+1)^4}{2n+1} \delta_{nn'} \delta_{mm'} \tag{14}$$

where $\Omega_{nm,n'm'}$ is an element of the matrix $\boldsymbol{\Omega}$, nm and $n'm'$ denotes the line and column indices, respectively, which are function of the degrees n and n' and of the orders m and m', and $\delta_{nn'}$ (resp. $\delta_{mm'}$) is the Dirac distribution equal to 1 when $n = n'$ (resp. $m = m'$) and 0 otherwise. The elements in Equation 14 are derived by computing analytically the diagonal elements of the following norm:

$$Q = \frac{1}{4\pi T} \int_T \int_\Omega \left\| \nabla_S^2 J_r(b, \theta, \phi, t, t_{UT}) \right\|^2 d\Omega dt \tag{15}$$

where Ω is equal to 4π and is the complete solid angle and T is one period equal to 1 year. The regularization matrix $\boldsymbol{\Lambda}$ gradually damps the energy in the high spherical harmonics degrees—similarly for each temporal mode—and smooths the final solution. It is crucial to obtain a clean mid and low latitude signal with minimum contamination from magnetospheric fields and minimum ringing originating from the strong high latitude signal propagating to lower latitudes. However, it is at the expense of smoothing small-scale structures and, therefore, to some extent, our model has a lower spatial resolution than an unregularized degree 60 model.

To determine a value for λ, we compute the three L curves for Model A, B, and C. In the following, we choose $\lambda = 5 * 10^{-2} \left(nA.m^{-4}\right)^{-2}$, a value close to the corners of all three L curves. For Model A, B, and C, an estimation of the model coefficients can be computed using:

$$\vec{m}^{est} = \left(\boldsymbol{G}^T \boldsymbol{C}_d^{-1} \boldsymbol{G} + \lambda \boldsymbol{\Lambda}\right)^{-1} \boldsymbol{G}^T \boldsymbol{C}_d^{-1} \vec{d} \tag{16}$$

We obtain three sets of coefficients that can be used to compute independent predictions of the South and East components of the toroidal field and of the radial component of the poloidal current inside the corresponding shells—blue and red shells in Figure 2—using Equations 4–6.

5. Magnetic Data Fit

We now discuss the model fit to the Swarm magnetic data. Here, it is important to keep in mind that, over the considered period of time, the Swarm satellites Alpha and Charlie orbit side by side in the same local time sector whereas at the same time Swarm Bravo orbits in a different local time sector. Therefore, the local time sector sampling is different for Swarm Alpha and Charlie on one side and Swarm Bravo on the other. By considering the data from each Swarm satellite as an independent dataset, this orbital configuration allows us to assess the robustness of the observed signal: first, with respect to the measurement errors—and possibly small-scale un-modeled field errors—and, second, with respect to the local time sector sampling. The first point can be assessed by comparing signals in Swarm Alpha and Charlie data. The second one by comparing signals in Swarm Alpha/Charlie and Swarm Bravo data.

The model is designed to represent the average diurnal and seasonal variations of F region magnetic fields; we first show that such an average signal exists in the data and that it is robust. To do so, we build maps of the average signal at each universal time and season using the preprocessed and selected data presented in Section 2. For each map, the data are further selected for one universal time and one season, respectively defined as a 1-hr window centered on the hour and a 3-month window centered on either one equinox or one solstice. The data are subsequently averaged inside bins of 5° of latitude by 5° of longitude. Note that these average data are only used for the purpose of visualization and are not the one used in Section 4 to build the model. Figure 3 shows an example of maps of the average magnetic field East and South components for all three Swarm satellites at 6:00 UTC in summer. At low and mid latitudes, the strongest signal is on the East component on the dayside and is about 15 nT in amplitude. This signal is observed in maps of all three Swarm satellites showing that it is robust. Around the magnetic equator, the East component is negative in the noon sector and positive in the morning and afternoon sectors. The sign is opposite at mid latitude. The low- and mid-latitude dayside signal on the South component is weaker, but we nevertheless observe similar signals in maps of all three satellites. It is negative around the magnetic equator in the noon sector and mostly positive at mid latitude in the morning, noon and afternoon sectors, with the exception of the morning sector in the Northern Hemisphere where it is negative. A significantly stronger signal is also observed at high latitude and at all local times on both the East and South components and for all three satellites. This signal is of the order of 80 nT. However, a climatological average makes less sense at these latitudes and one should expect significant variability around the climatological mean. Finally, meridional stripes can be observed at all local times on both the South and East components. Interestingly, these stripes are mostly similar for Swarm Alpha and Charlie, but different for Swarm Bravo. This suggests that they are not a climatological signal but rather a signature of fast varying signals. Such meridional signals most likely originate from residual magnetospheric fields. In the following, special care is taken to ensure that these signal are not contaminating the F region model.

Figures 4 and 5 show comparisons of maps of the data, of the model prediction and of the residuals for Swarm Alpha (left columns) and Swarm Bravo (right columns) respectively for the East and South components. The maps of the data and residuals are derived in the same way as the maps presented in Figure 3 using time series of the data and of the residuals—the difference between the data and the model prediction at each position and time—at 15:00 UTC in the summer. The maps showing model predictions are derived using predictions on a grid at 15:00 UTC on 20 June 2016. The corresponding maps for Swarm Charlie are very similar to those of Swarm Alpha (see Figure S1 in Supporting Information S1). On the East component (Figure 4), the average signal in the data is to some extent different to what was observed at 6:00 UTC in the summer (Figure 3). Here, the local midday is over South America where the magnetic equator dips. The dayside low- and mid-latitude signal follows the geometry of the magnetic equator, which supports its ionospheric origin. It is characterized by a negative patch over South America, between the morning and noon sectors, and three negative bands over the Atlantic Ocean, between the noon and afternoon sectors. As shown in Figure 4, the model East component reproduces well the average mid and low latitude dayside signal observed on the East component of the data for both Swarm Alpha and Bravo. On this component, the low- and mid-latitude dayside residuals are of the order of 5 nT, about one order of magnitude less than the signal in the data. Over the Pacific Ocean, on the night side, the model slightly overestimates the signal in the data which is reflected as positive residuals in this region. Figure 5 shows that the model fairly reproduces the overall morphology of the dayside signal on the South component of the data,
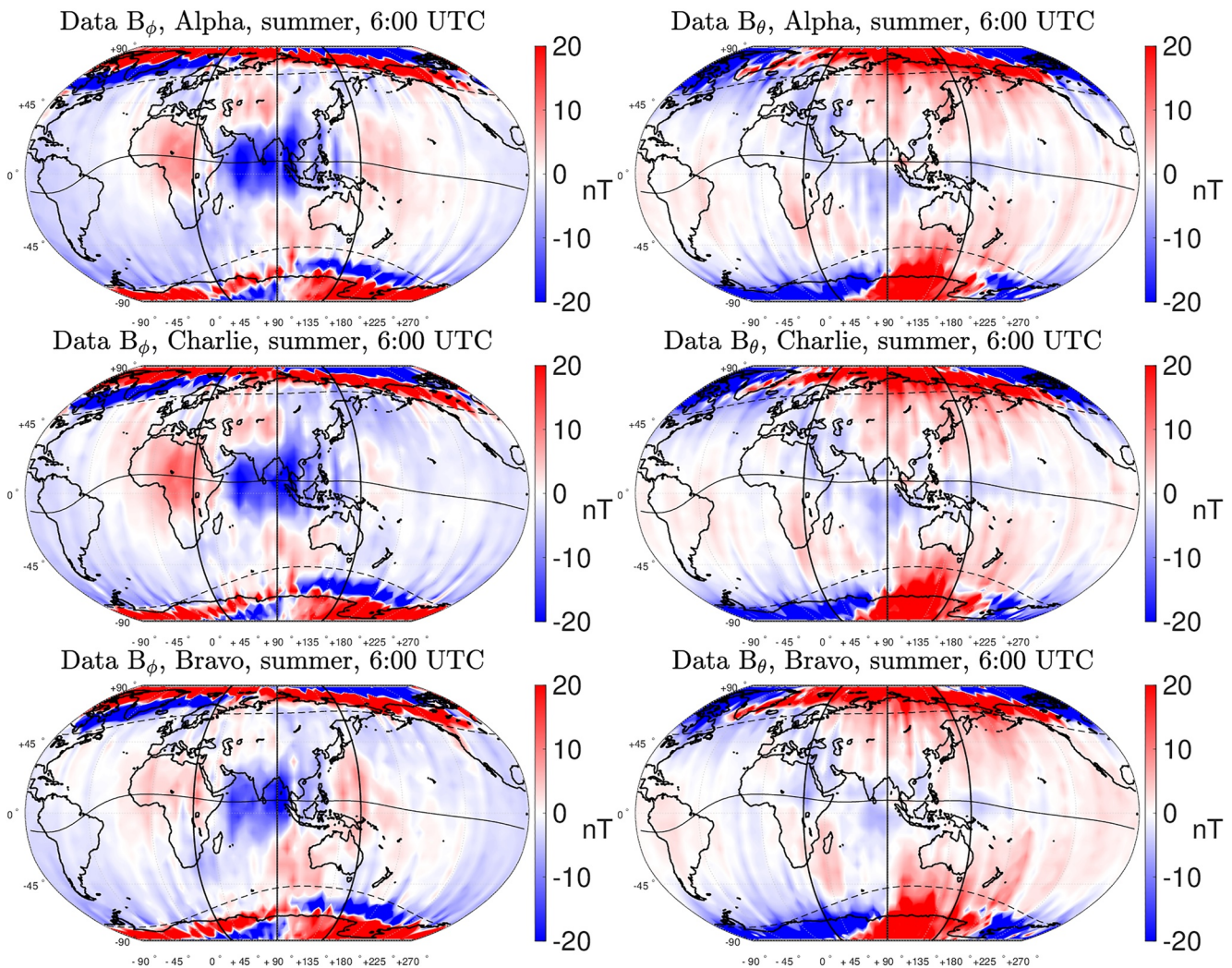
Figure 3. Maps of the average magnetic field East (left column) and South (right column) components derived with data from Swarm Alpha (first row), Charlie (second row) and Bravo (third row) at 6:00 UTC in summer. The magnetic equator is represented with a black plain line and the $\pm 60°$ quasi dipole parallels with two dotted lines. Three meridians are also represented and correspond to a local time of 8:00 (left), 12:00 (center) and 16:00 (right). The maps are centered on the local noon and the Robinson map projection is used—we keep the same two conventions for every map in this article.

although now slightly overestimating the signal in all local time sectors for both Swarm Alpha and Bravo. This could reflect the fact that the model optimizes the fit to the strongest signal, that is, the East component at low and mid latitude which is indeed stronger than the corresponding signal on the South component. At high latitude, the model captures the overall morphology of the signal on the South and East components for both Swarm Alpha and Charlie. However, the average residuals are quite significant in this region, of the order of 40 nT, reflecting the high variability of this signal which the climatological model cannot capture.

The results presented in Figures 3–5 show that the low- and mid-latitude dayside average signal is well captured by the model. These results are well representative of what is observed at all UTCs and seasons in maps of all three Swarm satellites. Overall, the low- and mid-latitude signal, mainly seen on the dayside East component, follows some significant climatological variations. Furthermore, as was already pointed out when discussing Figure 4, the signal is also well organized with respect to the main field geometry, which the model parametrization did not enforce.

6. Discussion

The three spherical harmonics representation—respectively labeled Model A, B, and C—can predict the radial component of the poloidal current density at the altitude of the Swarm satellites using Equations 6 and 10.
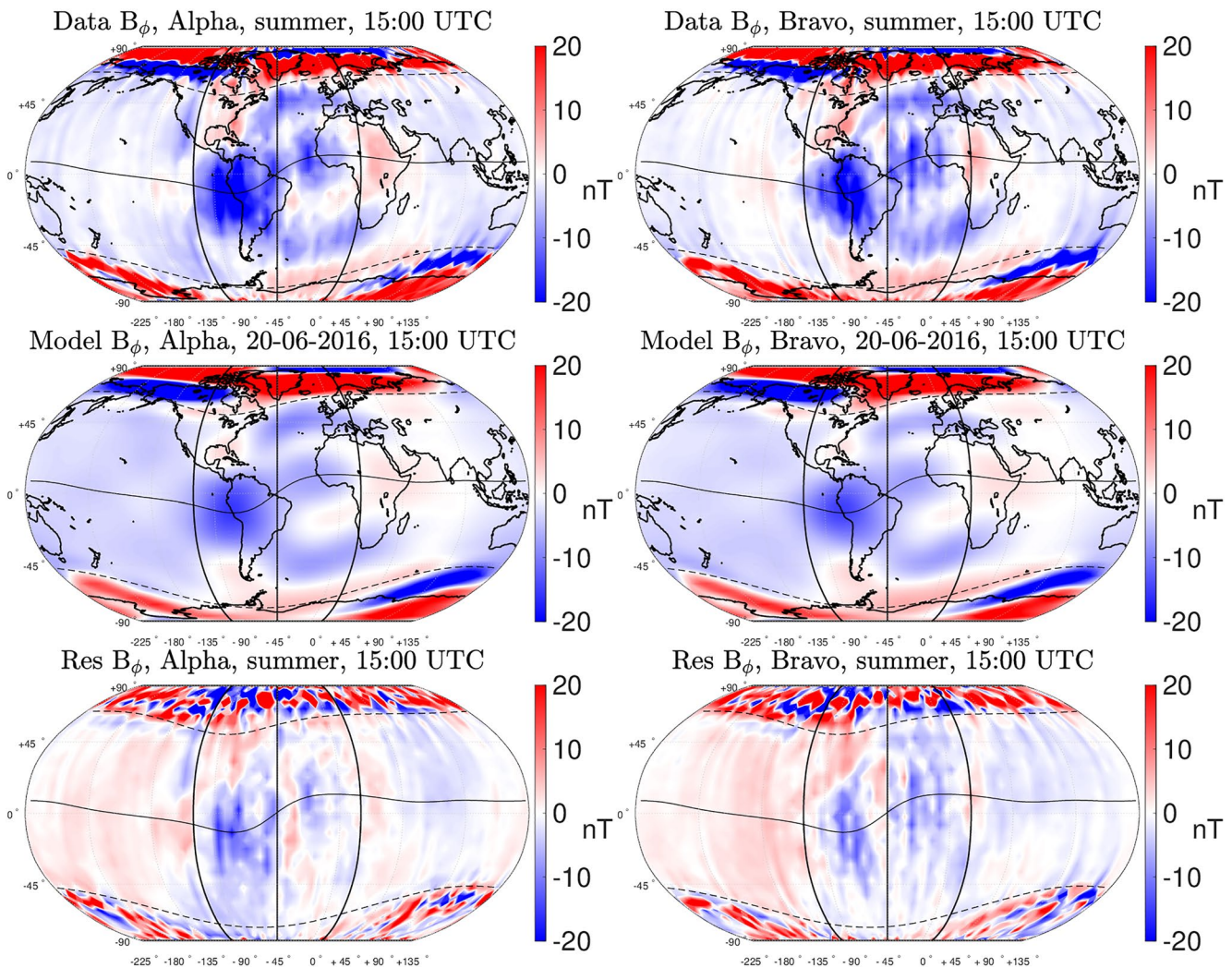
Figure 4. Maps of the east component of the data (first row), model prediction (second row) and residuals between the model and the data (third row) for Swarm Alpha (left column) and Swarm Bravo (right column). The data and residuals maps are derived using data at 15:00 UTC in summer. The model prediction map is derived using model prediction on a grid on 20 June 2016 at 15:00 UTC.

Therefore, they can be used to study the climatology of F region poloidal currents. In Section 6.1, we first discuss the ability of the model to reproduce well-known characteristics of these currents by comparing model predictions to results from previous studies. In Section 6.2, we use the model as a tool to provide a comprehensive view of F-region mid- and low-latitude ionospheric currents, which leads to new insight. In Section 6.3, we finally discuss the dynamics of F-region mid- and low-latitude ionospheric currents using integrated quantities.

6.1. Comparison With Previous Studies

Some of the most important characteristics of radial ionospheric F-region currents at low and mid latitudes are well summarized in Figures 1 and 2 of Park, Yamazaki, and Lühr (2020). These figures are built using single satellite estimates of the F-region ionospheric radial current density provided in the Level 2 Field-Aligned Current Swarm product (Ritter et al., 2013). Each figure consists of nine panels showing composite maps of the average radial current density built using data from one Swarm satellite at a specific magnetic local time (MLT) and season. We reproduce similar figures to evaluate if our model predicts realistic F-region currents.

Figures 6 and 7 present maps of the model predictions of the poloidal current radial component at several MLTs and days of year. These figures are designed to ease comparison with Figures 1 and 2 from Park, Yamazaki, and Lühr (2020). Each map is built in the following way. We first compute the radial poloidal current density
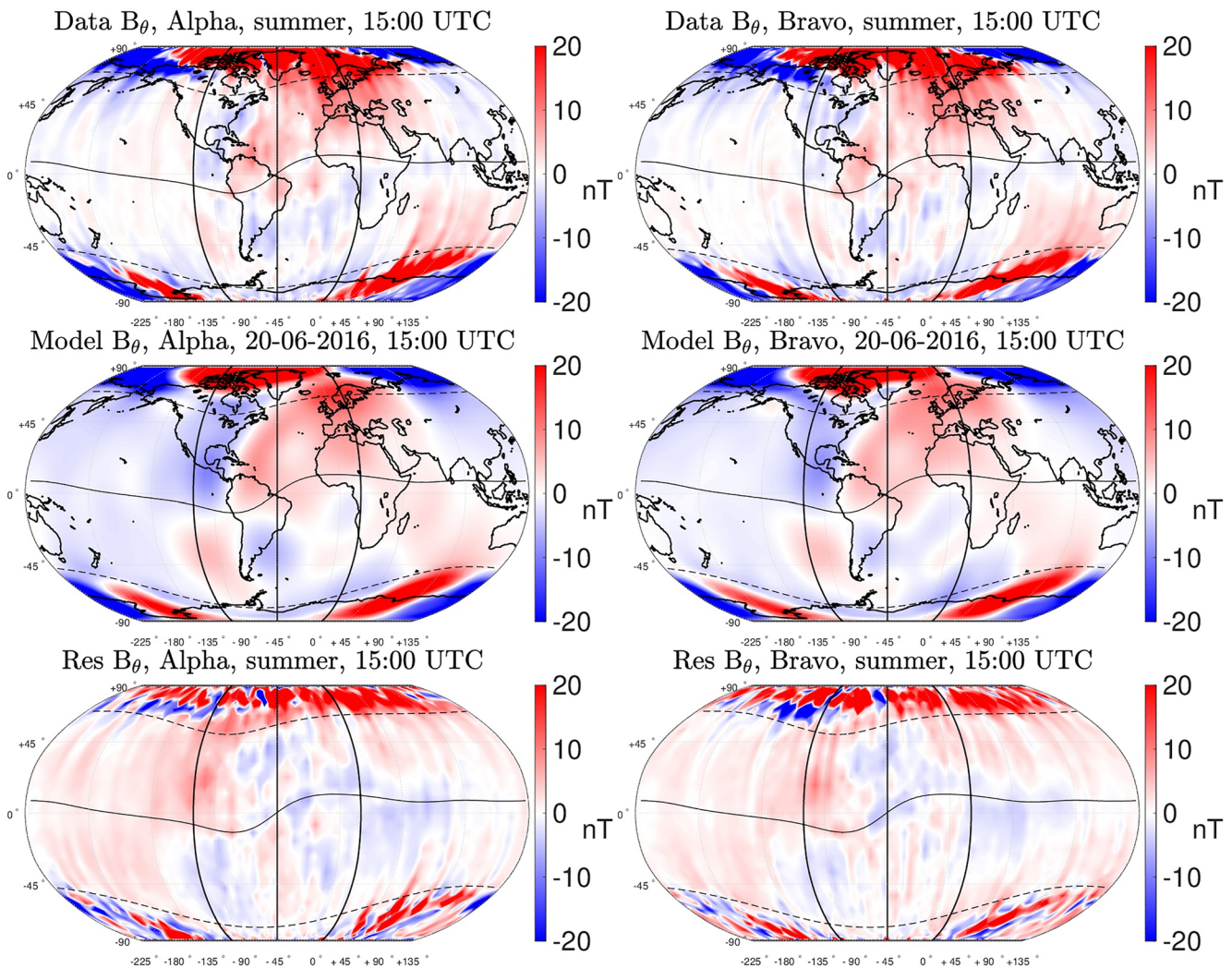
Figure 5. Same as Figure 4 for the South component.

prediction on a 5° × 5° grid covering the whole globe at each universal time during one appropriately chosen day. To represent the currents in spring, fall, summer and winter, the model predictions are computed on 20 March 2016; 22 September 2016; 20 June 2016; and 21 December 2016, respectively. For each individual day, the data are stacked together to form one dataset and we compute the MLT in quasi dipole coordinates for each individual data point. Finally, the data are selected for one specific MLT and the map is built by averaging these selected data in bins of 5° × 5°. Figure 6 shows maps built using Model A at 7:00 MLT (first column), 12:00 MLT (second column) and 16:00 MLT (third column) on 20 March 2016 (first row), 22 September 2016 (second row), 20 June 2016 (third row), and 21 December 2016 (fourth row). Figure 7 is the same figure for Model B. These two figures are to be compared with Figures 1 and 2 from Park, Yamazaki, and Lühr (2020). However, in this latter study, spring and fall seasons were considered together assuming that radial ionospheric F-region currents are the same during these seasons. Here, we considered them separately to assess potential differences. Finally, the results obtained with Model C—not shown—are very similar to those obtained with Model A (See Figure S2 in Supporting Information S1).

We first note the very good agreement between currents predicted by Model A (Figure 6) and Model B (Figure 7). This confirms again the robustness of the model with respect to data measurement errors and to data local time sampling. On both figures, the maps display radial F-region currents well organized with respect to the Earth's main field geometry and antisymmetric with respect to the magnetic equator. These are clear signatures of IHFACs well in agreement with maps from Park, Yamazaki, and Lühr (2020). Although these currents
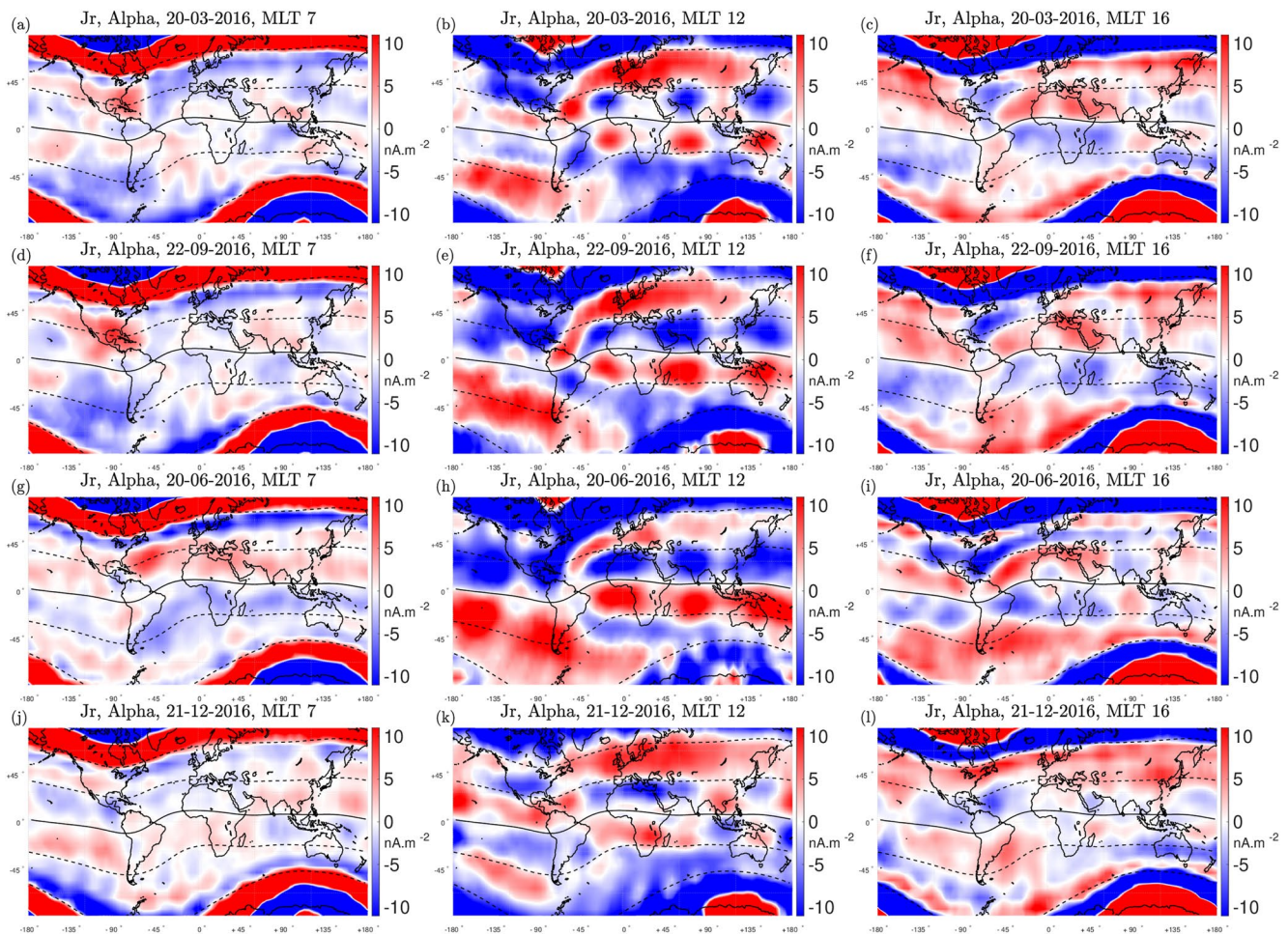
Figure 6. Maps of the radial poloidal current density predicted by Model A at 7:00 MLT (first column), 12:00 MLT (second column) and 16:00 MLT (third column) on 20 March 2016 (first row), 22 September 2016 (second row), 20 June 2016 (third row) and 21 December 2016 (fourth row). The quasi dipole magnetic equator is shown with a black plain line, and the $\pm 35°$ and $\pm 60°$ quasi dipole parallels with dashed lines.

generally dominate at low and mid latitudes, one should keep in mind that other second-order currents could also contribute. This is particularly true above the magnetic equator where radial dynamo currents have been identified (Lühr et al., 2019; H. Wang, Lühr, et al., 2022). IHFACs fall in two categories: low-latitude IHFACs, which roughly flow in a latitude band between the magnetic equator and the $\pm 35°$ magnetic parallels, and mid-latitude IHFACs, which roughly flow between $-60°$ and $-35°$ in the Southern Hemisphere and $35°$ and $60°$ in the Northern Hemisphere. It is worth noting that most previous studies mainly focused on low-latitude IHFACs (Abidin et al., 2019; Lühr et al., 2015, 2019; O. P. Owolabi et al., 2018; Park et al., 2011; Shinbori et al., 2017; Yamashita, 2002) whereas mid-latitude IHFACs were only brought to light recently (Fathy et al., 2019; Park, Yamazaki, & Lühr, 2020).

We start by discussing currents at low latitude. The low-latitude IHFACs in the morning sector—left columns of Figures 6 and 7—are generally weak, of the order of 1–5 nA.m^{-2}. In spring and fall—panels (a) and (d), these currents exhibit clear polarity in the American and Pacific Ocean sectors, where they are mostly southbound between $-135°$ and $-45°$ of longitude and mostly northbound between $-180°$ and $-135°$ of longitude, and in the Indian Ocean sector, between $+45°$ and $+90°$where they are mostly southbound. In summer—panels (g), the morning low-latitude IHFACs are southbound at almost all longitudes, which agrees with results from Lühr et al. (2019), except around $-90°$ of longitude where they are northbound. In contrast, the morning winter low-latitude IHFACs—panels (j)—are mostly northbound between $-180°$ and $50°$ of longitude and southbound between $50°$ and $180°$ of longitude.

The low-latitude IHFACs in the noon sector—center columns of Figures 6 and 7—are significantly stronger in comparison to their morning sector counterpart. They are of the order of 10–15 nA.m^{-2}. It is interesting to
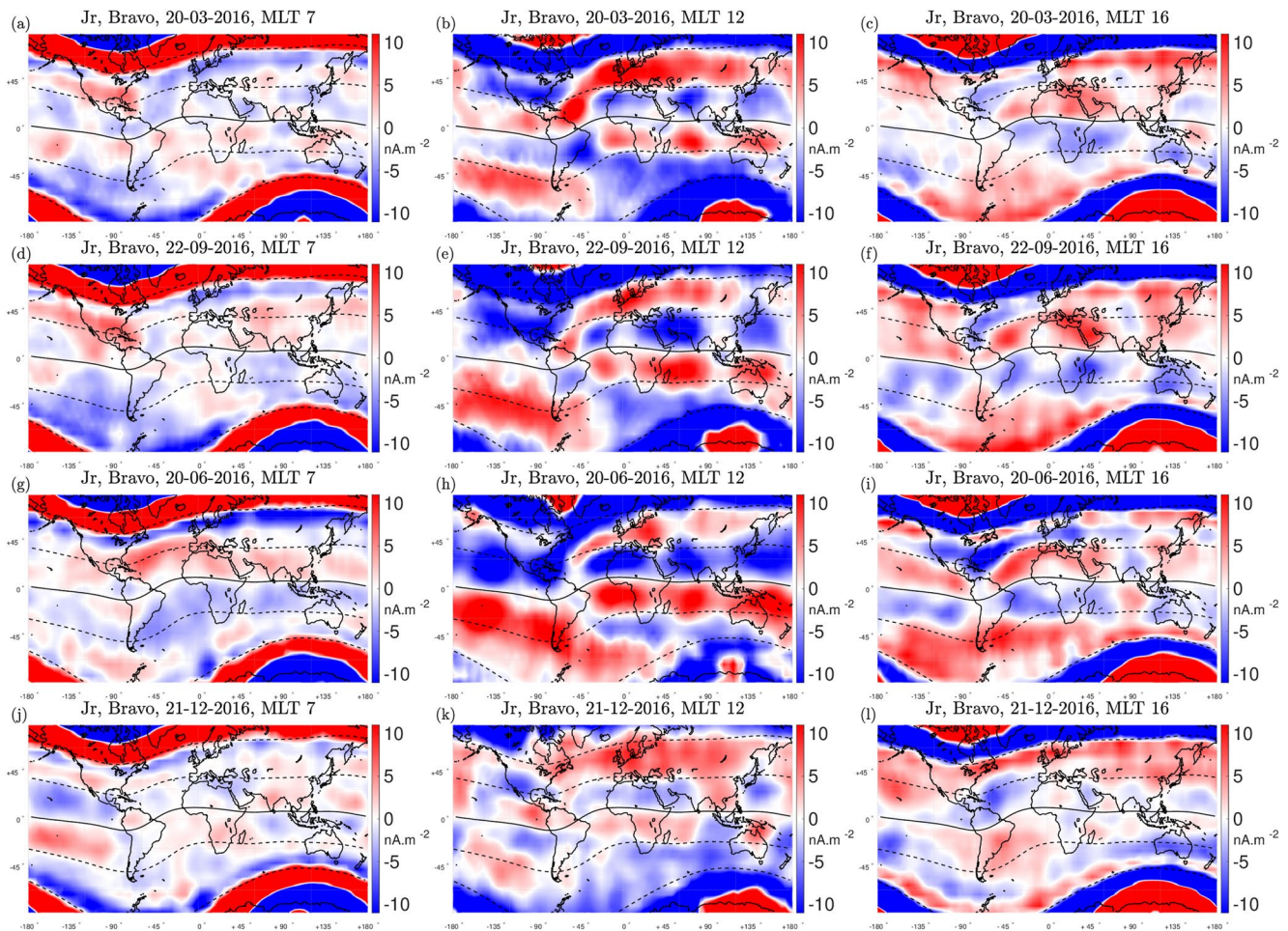
Figure 7. Same as Figure 6 for Model (b).

compare these currents in spring and fall—panels (b) and (e)—as IHFACs during these two seasons are often considered similar. Comparison of these two seasons in Figures 6 and 7 shows that this is only partly true. Indeed, stronger noon low-latitude IHFACs are predicted by the model in fall than in spring at all longitudes. The low-latitude IHFACs in fall and spring both flow northbound East of the magnetic equator dip—between −30° and 180° of longitude. However, they have a different polarity West of the magnetic equator dip, that is between −180° and −80° of longitude: they are mostly northbound in fall and southbound in spring. In summer—panels (h), we observe clear northbound noon low-latitude IHFACs at almost all longitudes consistently with all the studies cited above. Interestingly, the polarity is reversed over Brazil in the region of the South Atlantic Anomaly (SSA)—between −60° and −30° of longitude—which is also observed in Figures 1 and 2 of Park, Yamazaki, and Lühr (2020). Finally, the case of noon low-latitude IHFACs in winter is interesting as these currents are historically not well constrained. They were first believed to flow southbound following Fukushima's conceptual model (Fukushima, 1994). However, recent studies show that this model does not hold for winter (Lühr et al., 2019; Park, Yamazaki, & Lühr, 2020) and that the current pattern for this season remains unclear. Our results—panels (k)— show that extracting the winter pattern from Swarm data is possible. The low-latitude winter IHFACs display a rather complicated pattern. They flow southbound over most of the Pacific Ocean, Central and South America, and northbound over most of the Atlantic Ocean, Africa and the Middle East, which agrees with results obtained by Lühr et al. (2019). Additionally, we observe an abrupt change of polarity over East Asia—between 90° and 130° of longitude—and in the Japan-Australia sector—between 130° and 170° of longitude—: the currents flow southbound over the first and northbound over the second.

The low-latitude IHFACs in the afternoon sector—right columns of Figures 6 and 7—are weaker compared to those in the noon sector and generally flow in the opposite direction. This agrees well with some of the

most recent studies (Lühr et al., 2019; Park, Yamazaki, & Lühr, 2020). Additionally, the low-latitude afternoon IHFACs are stronger than their morning counterparts at all seasons, as they are of the order of 4–7 nA.m^{-2}. In spring and fall—panels (c) and (f) -, these currents mostly flow southbound. They are almost similar during these two seasons, with only minor differences such as in the SAA sector—around −80° of longitude—where the low-latitude IHFACs are northbound in spring whereas we observe both northbound and southbound low-latitude IHFACs in fall. In summer—panels (i) -, the afternoon low-latitude IHFACs are southbound except around +90° where they are northbound. In winter—panels (l), the afternoon low-latitude winter IHFACs is mostly northbound, except over Africa, between 0° and 40° of longitude, East Asia, between 100° and 140°and over the Pacific Ocean, between −180° and −145°where they are mostly southbound.

The well documented tidal longitudinal modulation of noontime low-latitude IHFACs is also observed in Figures 6 and 7. This modulation is particularly marked in summer—panels (h). It is generally believed that the associated variations are characterized by a wave number-4 (WN-4) structure (Lühr et al., 2019; Park et al., 2011), however, results here rather suggest a WN-5 structure as suggested by Park, Yamazaki, and Lühr (2020). The WN-5 pattern can also be observed in Figure 8e of Park, Stolle, et al. (2020). A similar longitudinal modulation is also observed at noon in fall and spring—panels (b) and (e). During these two seasons, the low-latitude IHFACs display a clear three-peak tidal modulation East of the equatorial dip, between −45° and +180° of longitude. However, no clear modulation is observed west of it. Similarly, no clear modulation is observed at noon in winter—panels (k)—or at all seasons in the morning and afternoon sectors—first and third columns of Figures 6 and 7. It is also worth noting that the C-shaped structure starting in the North Atlantic down to South America in summer and equinox seasons reported by Park, Stolle, et al. (2020) is also well reproduced by the model, as can be observed in panels (b), (e), and (h).

We now turn to mid-latitude IHFACs. The observed structure for these currents is simpler compared to their low latitude counterparts. In the morning sector—first columns of Figures 6 and 7, the mid-latitude IHFACs are generally weak. Interestingly, in this sector, we observe two narrow bands of negative currents covering all longitudes: one right below the +60° quasi dipole parallel in the Northern Hemisphere and the other right above the −60° quasi dipole parallel in the Southern Hemisphere. This is not a signature of IHFACs as these currents are not antisymmetric with respect to the magnetic equator. Furthermore, they were not observed in Figures 1 and 2 of (Park, Yamazaki, & Lühr, 2020). These currents could be artifacts of the model, reflecting the difficulty to represent mathematically the sharp transition between low- and mid-latitude IHFACs and high-latitude field-aligned currents, or possibly other radial ionospheric currents.

In the noon sector—second columns of Figures 6 and 7 -, the mid-latitude IHFACs do not vary significantly with season. As already observed by (Park, Yamazaki, & Lühr, 2020), their polarity is generally opposite in comparison with low latitude IHFACs, although this is not systematically the case as, for instance, in the noon sector in fall and summer—panels (e) and (h)—between −180° and −80° of longitude. Furthermore, we do not observe a similar longitudinal modulation of mid-latitude IHFACs compared to low-latitude IHFACs, as was also reported by Park, Yamazaki, and Lühr (2020). They are mostly northbound between −150° and −45° of longitude and southbound everywhere else, which is consistent with observations from Park, Yamazaki, and Lühr (2020). Finally, in the afternoon sector—third columns of Figures 6 and 7, the mid-latitude IHFACs seems to be mostly southbound in fall, spring and winter—panels (c), (f) and (l)—, and mostly northbound in summer—panels (i). It is worth noting that, similarly to what was observed in the morning sector, we observe in this sector two narrow bands of positive potential artifact currents close to the ±60° quasi dipole parallels.

The analysis of the signal observed in Figures 6 and 7 showed that the Model A, B, and C reproduces well-known characteristics of F-region low- and mid-latitude IHFACs and provide new insight. It is worth noting, however, that other important F-region electric currents exist, such as the well-documented meridional dynamo currents flowing in a narrow band around the magnetic equator (Lühr & Maus, 2006; Lühr et al., 2019; H. Wang, Lühr, et al., 2022). These currents are not captured by the model. This is because a higher spatial resolution would be necessary, which is prevented by the smoothing regularization term—Equation 15—used in the inversions. The model can still be used to study low- and mid-latitude IHFACs. Looking at the signal at selected MLTs, however, has some inherent limitations, as one must assume that the current system is fixed with respect to MLT to provide a correct interpretation. In the next sections, we take advantage of the full capabilities of the model to investigate the dynamics of low- and mid-latitude IHFACs.
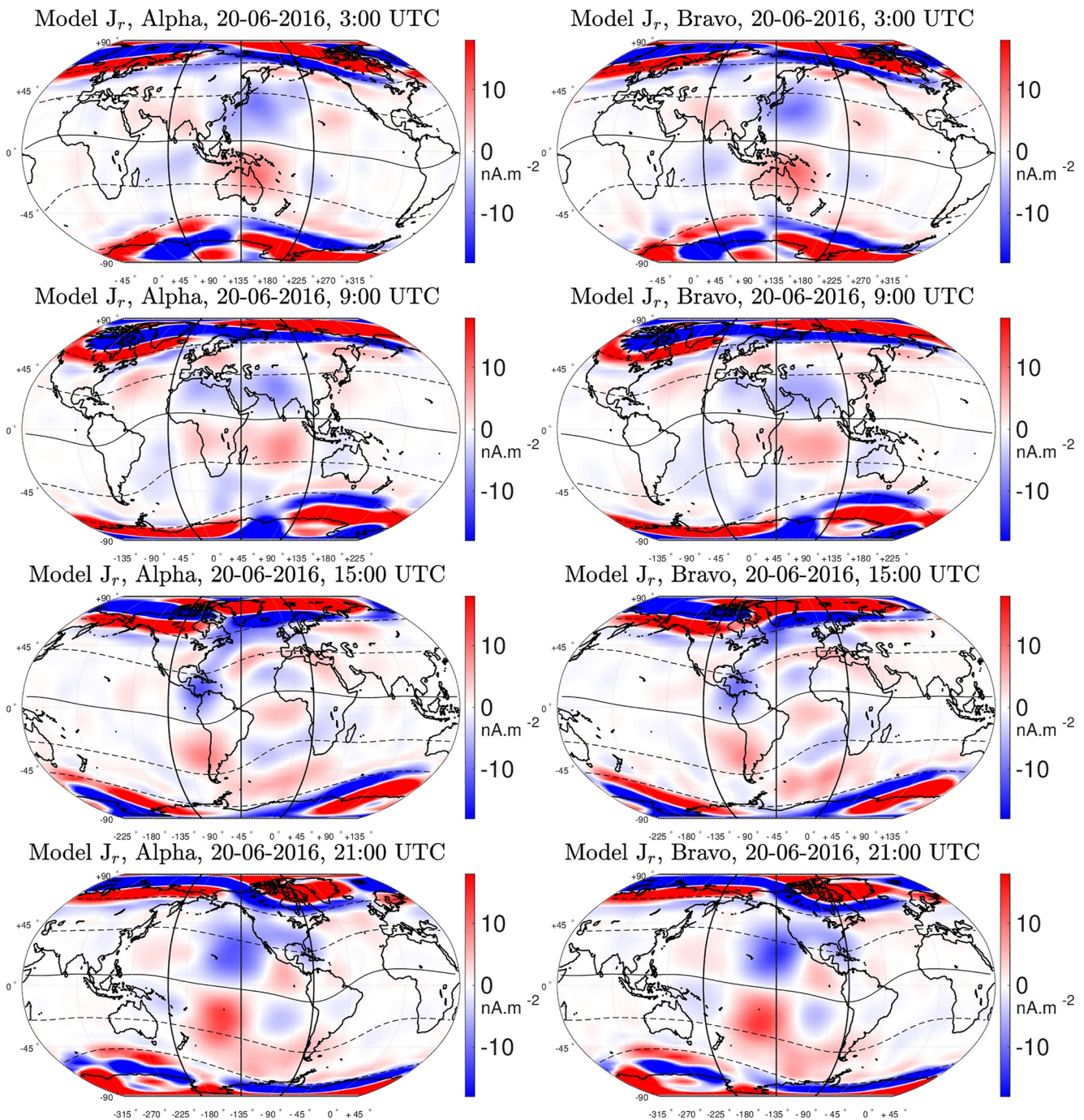
Figure 8. Maps of the radial poloidal current density predicted by Model A (first column) and Model B (second column) at 3:00 UTC (first row), 9:00 UTC (second row), 15:00 UTC (third row) and 21:00 UTC (fourth row) on 20 June 2016—which corresponds to the summer solstice. The quasi dipole magnetic equator is shown with a black plain line, and the $\pm 60°$ and $\pm 35°$ quasi dipole parallels with dashed lines.

6.2. A Comprehensive View of IHFAC Climatology

The F-region radial poloidal currents can also be studied by directly looking at successive maps representing these currents predicted by Model A, B, and C at a selected UTC. This representation provides additional insight. In Sections 6.2.1, 6.2.2, and 6.2.3, we use this representation to provide a comprehensive view of the climatology of IHFACs. We first discuss the daily variations in summer in Section 6.2.1 and in winter in Section 6.2.2. We then discuss the seasonal variations using examples at two selected UTCs in Section 6.2.3. In all these sections,

we have distinguished between low- and mid-latitude IHFACs using the $+35°$ quasi dipole parallel in the Northern Hemisphere and the $-35°$ quasi dipole parallel in the Southern Hemisphere.

6.2.1. Daily Variations of IHFACs in Summer

Figure 8 shows maps of the radial poloidal current predicted by Model A (left column) and Model B (right column) at 3:00 UTC (first row), 6:00 UTC (second row), 15:00 UTC (third row) and 21:00 UTC (fourth row) on 20 June 2016—which corresponds to the summer solstice. All maps are centered on the meridian corresponding to the noon local time. In Figure 8, consistently with what was already noted in Section 6.1, a clear low- and mid-latitude signal of IHFACs equatorward of the $\pm60°$ quasi dipole parallels is seen which is antisymmetric with respect to the magnetic equator. Poleward of the $\pm60°$ quasi dipole parallels, we also observe the signatures of high-latitude field-aligned currents. These currents will not be discussed in this section—or in any of the following sections—as the focus of this paper is on mid and low latitudes.

The succession of maps at 3:00 UTC, 9:00 UTC, 15:00 UTC and 21:00 UTC provides a clear view of the longitude variations of low- and mid-latitude IHFACs in summer. A conspicuous feature is the different structure of IHFACs observed in maps at 15:00 UTC—third row of Figure 8—compared to the other maps. This UTC corresponds to a time when the dayside is over the region of the South Atlantic Anomaly (SSA), where the geometry of the main field is distorted. In this region, the IHFACs seem to flow in two sectors. The first sector is the late morning sector, at about $-70°$ of longitude, where the model predict northbound IHFACs at both low and mid latitudes. The second sector encompasses the noon and afternoon sectors—roughly between $-45°$ and $90°$ of longitude—where the structure of IHFACs is more complex. In contrast, in maps at 3:00 UTC, 9:00 UTC and 21:00 UTC—corresponding to UTCs when the dayside is over regions where the geometry of the main field is less distorted, the morphology of IHFACs at low latitude is rather simple. To first order, it can be described as follows: low-latitude IHFACs are southbound in the morning sector, northbound in the noon sector and southbound in the afternoon sector. These observations highlight the importance of the main field's geometry as was previously noted by Le Sager and Huang (2002) using numerical simulations.

Another interesting feature appears when considering the local current density maximum of low-latitude IHFACs in the noon sector. A close inspection of maps in Figure 8 shows that this maximum does not always coincide with the meridian corresponding to noon. This can be particularly observed on the maps at 3:00 UTC and 9:00 UTC—first and second rows of Figure 8. In these maps, the meridian marking the noon local time—center black meridians in Figure 8—can be taken as a good approximation of the noon MLT meridian given that the magnetic equator is relatively flat in these sectors. In maps at 3:00 UTC, the current density maximum in the noon sector is located at about $+150°$ of longitude whereas the meridian marking the noon local time is at $+135°$. In maps at 9:00 UTC, the low-latitude IHFACs around the noon sector has two local current density maximums: one in the late morning sector, at about $30°$ of longitude, and another in the early afternoon sector, at about $80°$ of longitude—the noon meridian is this time at $+45°$. In contrast, the current density maximum in the noon sector in maps at 21:00 UTC—fourth row of Figure 8—seems much more aligned with the meridian marking the noon local time—at about $-135°$ of longitude -, although the magnetic equator is tilted in this sector making this observation less reliable. Taken all together, these observations nevertheless suggest that a substantial part of low-latitude IHFAC variations with longitude is not in phase with the Sun. This specific issue will be discussed more in Section 6.3.

Figure 8 also provides some insight on IHFAC variations with latitude. As mentioned in Section 6.1, mid-latitude IHFACs were only identified in recent studies (Fathy et al., 2019; Park, Yamazaki, & Lühr, 2020). These currents are thought to frequently be of opposite polarity compared to their low-latitude counterparts. In maps at 3:00 UTC, the model does not predict any significant mid-latitude IHFACs with opposite polarity at this UTC. This shows that mid-latitude IHFACs with opposite polarity are not systematic. In contrast, we observe northbound low-latitude IHFACs together with southbound mid-latitude IHFACs on the maps at 9:00 UTC, which this time is well in agreement with Park, Yamazaki, and Lühr (2020). Furthermore, the case of the map at 15:00 UTC is particular. In these maps, we see a pattern of three IHFAC systems with alternating opposite polarity in the noon and afternoon sectors—roughly between $-45°$ and $90°$ of longitude—. The first pattern is located close to the magnetic equator and consists in northbound IHFACs. The second one can be observed on the $\pm35°$ quasi dipole parallels and consists in southbound currents. The third one is located close to the $+60°$ quasi dipole parallel in the Northern Hemisphere and close to the $-60°$ parallel in the Southern Hemisphere and consists in northbound IHFACs. The fact that the polarity of IHFACs at low and mid latitudes can change more than one time is reported

in this study for the first time. Finally, we also observe southbound low-latitude IHFACs together with northbound mid-latitude IHFACs in maps at 21:00 UTC in the early afternoon sector—at about −90° of longitude. This configuration, however, is limited to this local time sector as no mid-latitude IHFACs with opposite polarity are observed in the other local time sectors.

The analysis of maps in Figure 8 made it possible to highlight several important characteristics of IHFACs in summer. It first confirms that IHFACs can change polarity with latitude as shown by Park, Yamazaki, and Lühr (2020). However, this is not systematic and these variations with latitude seems to be mostly confined to specific local time sectors. Furthermore, IHFACs can change polarity with latitude more than one time as shown in maps at 15:00 UTC. The analysis also showed that low- and mid-latitude IHFACs follow significant variations with longitude as previously discussed in numerous studies (Lühr et al., 2015, 2019; Park et al., 2011; Park, Yamazaki, & Lühr, 2020). Part of these variations is related to variations of the main Earth's magnetic field geometry. Another part is not in phase with the Sun and seems to be driven by another physical mechanism. The latter will be further discussed in Section 6.3.

6.2.2. Daily Variations of IHFACs in Winter

Figure 9 is the same as Figure 8 but for radial poloidal currents predicted by Models A and B on 21 December 2016, which corresponds to the winter solstice. As already mentioned in Section 6.1, the winter IHFACs is historically not well constrained. For the first time, Figure 9 gives a clear picture of IHFAC daily variations in winter. As a first general comment, we observe weaker IHFACs compare to summer, which agrees with some conclusions in previous studies (Lühr et al., 2019; Park, Yamazaki, & Lühr, 2020).

The Fukushima's conceptual model is often taken as a reference to provide a quick diagnostic of IHFACs climatology (Fukushima, 1994). This model states that low-latitude IHFACs flow from the summer hemisphere to the winter hemisphere in the morning sector, and from the winter hemisphere to the summer hemisphere in the noon sector. Recent studies, however, have shown that this conceptual model might not be valid for winter—see also Section 6.1—(Lühr et al., 2019; Park, Stolle, et al., 2020; Park, Yamazaki, & Lühr, 2020). Our results for winter— Figure 9—indeed reveal much more complex structure of IHFACs in this season. A good example is given in maps at 3:00 UTC in Figure 9—first row. At low-latitude, IHFACs mostly flow in the same direction as their summer counterparts, that is southbound in the morning sector—between 60° and 100° of longitude -, northbound in the noon sector—here roughly between 135° and 180° -, and southbound in the afternoon sector—at about 195° of longitude. This is in contradiction with Fukushima's model. The mid-latitude IHFACs, however, are significantly different from their summer counterparts, as we observe southbound IHFACs in almost all local time sectors on the dayside which were not observed in summer. Another interesting example can be observed in maps at 9:00 UTC— second row of Figure 9. In these maps, to first order, both low- and mid-latitude IHFACs flow in the same direction as their summertime counterparts, being again in direct contradiction with Fukushima's conceptual model.

IHFACs in winter follow some significant variations with longitude, similarly to what was observed in summer. The maps at 15:00 UTC, corresponding to a time when the dayside is over a region where the main field is the most distorted, show again the important role played by the geometry of the main field. Indeed, the morphology of IHFACs in these maps is significantly different to what can be observed in maps at 3:00 UTC, 9:00 UTC and 21:00 UTC. Additionally, and again similarly to what was noted in summer, we observe that the current density maximums in the noon sector do not always coincide with the meridians corresponding to the noon local time. This can be well observed in maps at 3:00 UTC, in which the maximum is at about +150° of longitude whereas the noon meridian is at +135° of longitude, and in maps at 9:00 UTC, in which the maximum is around +30° of longitude and the noon meridian at +45° of longitude. This aspect will be discussed in Section 6.3.

The maps produced by Model A and B—and C, not shown here (see Figure S3 in Supporting Information S1)—in Figures 8 and 9 generally show very good agreement. This is in line with conclusions from Sections 5 and 6.1. A close inspection of these maps, however, show that some small differences exist. This is particularly true for the maps at 21:00 UTC in winter—fourth row of Figure 9. In these maps, in the noon sector—at about −140° of longitude, we observe clear southbound low-latitude IHFACs together with northbound mid-latitude IHFACs for Model A whereas we only observe northbound mid-latitude IHFACs and no clear low-latitude IHFACs for Model B. This difference could possibly be explained by the different local time sampling of Swarm satellite Alpha and Bravo over the considered period of time in this study.

The maps in Figure 9 show the complex dynamics of IHFACs in winter. Similarly to summer, winter IHFACs follow some significant variations with longitude in relation with both the main field geometry and a longitudinal
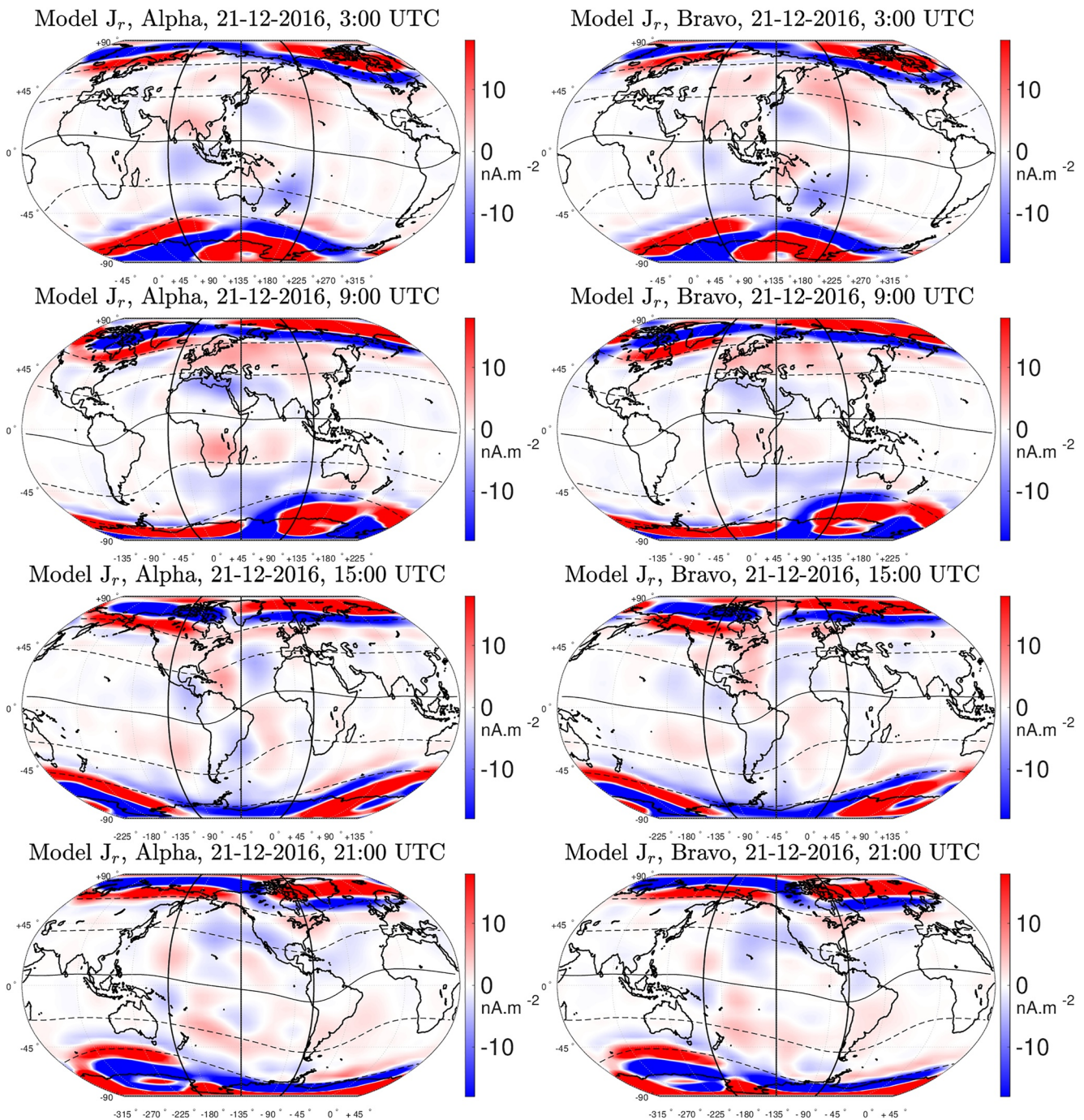
Figure 9. Same as Figure 8 but on 21 December 2016—which corresponds to the winter solstice.

modulation which is not in phase with the Sun. Furthermore, a close comparison of maps in Figures 8 and 9 show that, although there are some clear morphological differences between winter and summer, the IHFACs in these two seasons often flow in the same direction. This observation is in contradiction with Fukushima's conceptual model. Our results show that winter IHFACs follow some complex variations which are not fully understood.

6.2.3. Two-Season Behavior of IHFACs

Whereas the IHFAC configurations are significantly different in winter and summer, the configurations during equinox seasons, on the other hand, are believed to be close to the summer one (Lühr et al., 2019; Park, Yamazaki,
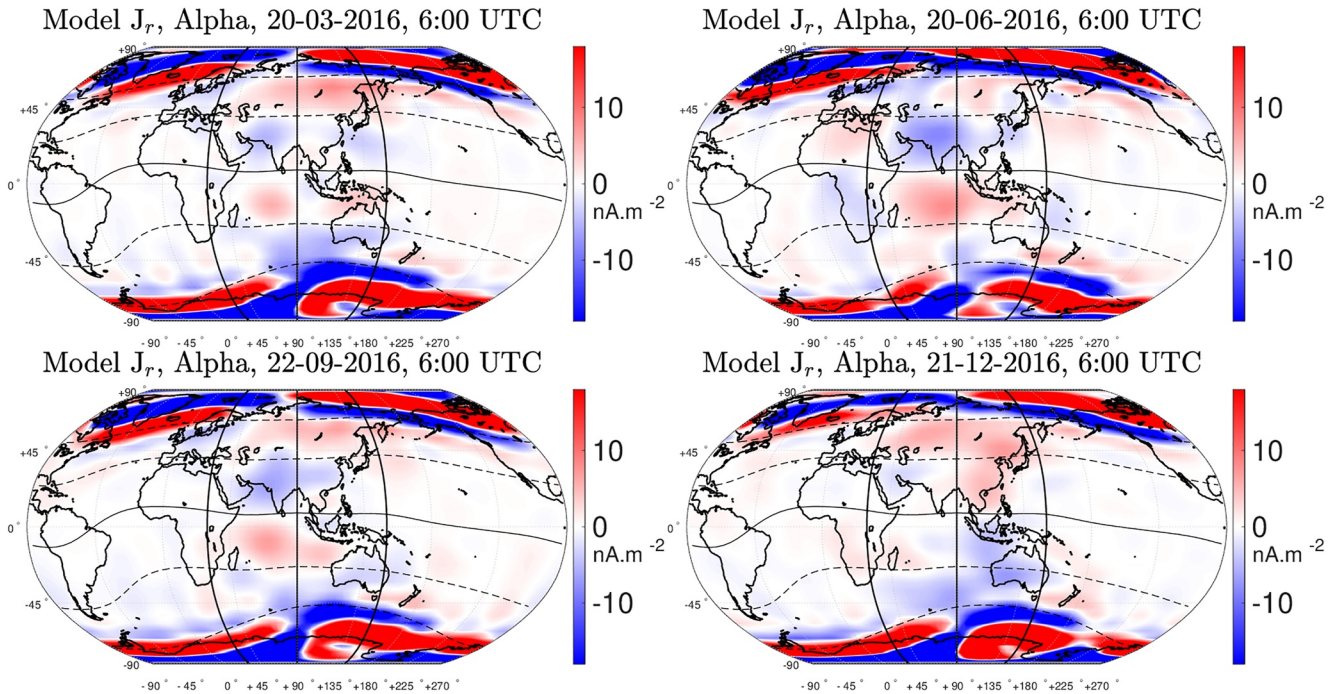
Figure 10. Maps of the radial poloidal current density predicted by Model A at 6:00 UTC on 20 March 2016 (spring equinox, upper left panel), on 20 June 2016 (summer solstice, upper right panel), on 22 September 2016 (fall equinox, bottom left panel) and on 21 December 2016 (winter solstice, bottom right panel). The quasi dipole magnetic equator is shown with a black plain line, and the $\pm 35°$ and $\pm 60°$ quasi dipole parallels with dashed lines.

& Lühr, 2020). This seasonal variation is sometimes called the two-season behavior of low- and mid-latitude IHFACs (Park, Yamazaki, & Lühr, 2020). To some extent, our results in Section 6.1 confirms the two-season behavior of IHFACs, although we could still identify some clear differences between IHFACs in fall, spring, and summer. In this section, we further discuss the two-season behavior using the model derived in this study. As it would be too tedious to show and discuss maps for all seasons, all UTCs, and Model A, B, and C, we selected two examples of seasonal variations predicted by Model A at two different UTCs. These two examples, while not exhaustive, give a good sense of how IHFACs vary with season. The corresponding maps for Model B and C show very similar IHFACs.

Figures 10 and 11 show maps of the radial poloidal current predicted by Model A respectively at 6:00 UTC and 18:00 UTC on 20 March 2016 (spring equinox, upper left panel), 20 June 2016 (summer solstice, upper right panel), 22 September 2016 (fall equinox, bottom left panel) and 21 December 2016 (winter solstice, bottom right panel)—see also Figures S4 and S5 in Supporting Information S1 for similar maps produced with Model B and C. The maps in Figure 10 corresponds to a UTC when the dayside is in a longitude sector where the Earth's main magnetic field is not too distorted. Figure 11, on the other hand, show maps at 18:00 UTC when the dayside is in the longitude sector close to the SAA, that is where the Earth's main magnetic field geometry is more distorted.

The IHFACs in falls and spring in Figures 10 and 11—first columns—have very close morphologies. In maps at 6:00 UTC—Figure 10, first column -, we observe northbound low-latitude IHFACs together with southbound mid-latitude IHFACs in a longitude range which roughly goes from 30° to 145°—roughly corresponding to late morning, noon and early afternoon sectors—in both spring and fall. On the maps at 18:00 UTC—Figure 11, first column, we observe northbound low-latitude IHFACs together with southbound mid-latitude in a longitude range going from −180° to −80°—roughly the morning and late morning sectors—again for both fall and spring. Interestingly, the configuration seems to be reversed in the longitude sector ranging from −80° to 45°—roughly the noon, early afternoon and afternoon sectors—as we observe southbound low-latitude IHFACs together with northbound mid-latitude IHFACs also for both equinox seasons. More generally, IHFACs in fall seems to be stronger than their spring counterpart, which confirms some first observation made in Section 6.1. This specific point will be further discussed in Section 6.3.

The IHFACs in summer in Figures 10 and 11—upper right panels—are indeed very similar to their fall and spring counterparts, as suggested by the two-season behavior hypothesis. We could, however, spot two important differences.
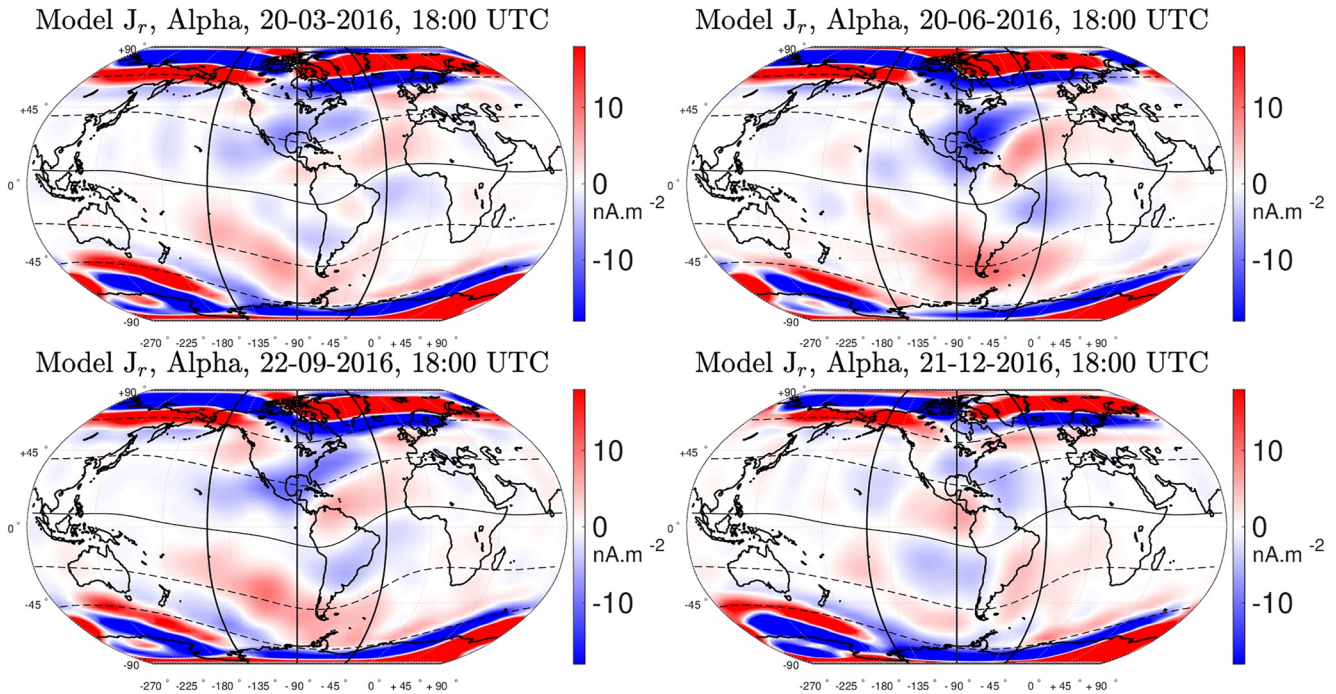
Figure 11. Same as Figure 10 but at 18:00 UTC.

First, the IHFACs in summer seems to be stronger than in fall and spring—which will be further discussed in Section 6.3. Second, the low-latitude IHFACs in the morning sector are different in summer. In maps at 6:00 UTC—Figure 10, upper right panel, we observe southbound low-latitude IHFACs in a longitude range going from −45° to 0°—roughly the early morning sector—which could not be observed in fall and spring—Figure 10, first column. In maps at 18:00 UTC—Figure 11, upper right panel, we observe much weaker northbound low-latitude IHFACs in the morning sector—at about −150° of longitude—compared to their fall and spring counterparts—Figure 11, first column. Additionally, on this same map, we also observe weak southbound low-latitude IHFACs in the early morning sector—at about −180° of longitude—which could not be observed on the corresponding maps in fall and spring.

The IHFACs in winter in Figures 10 and 11—bottom right panels—are significantly different from their summer, fall and spring counterparts. On the map at 6:00 UTC—Figure 10, bottom right panel, we see northbound low-latitude IHFACs together with southbound mid-latitude IHFACs in a longitude sector ranging from +20° to +70°—roughly the morning and late morning sectors. In the longitude sector ranging from +70° to +150°—roughly the noon and early afternoon sectors, we observe southbound IHFACs at both low and mid latitudes. The configuration is different for the winter IHFACs on the map at 18:00 UTC—Figure 11, bottom right panel. In this map, we observe northbound low-latitude IHFACs in the morning sector—at about −150° of longitude; southbound low-latitude IHFACs together with northbound in a longitude range ranging from −135° to −30°—roughly the late morning and noon sectors; and northbound IHFACs at about +40°—roughly the early afternoon sector—at both low and mid latitudes.

The observation of Model A current density predictions in Figures 10 and 11 generally confirms the two-season behavior of IHFACs. This two-season behavior, however, is only a first order approximation as some substantial differences could be observed in maps in fall, spring and summer.

6.3. Analysis of IHFAC Dynamics Using Integrated Quantities

The analysis of the maps presented in Sections 6.2.1, 6.2.2 and 6.2.3 have provided some interesting new insight on IHFAC climatology. In these maps, however, it is difficult to grasp a good sense of the overall dynamics. A good alternative to current density maps is to use an integrated quantity that would summarize the information contained in maps at all UTCs and seasons. An appropriate quantity is the total amount of current, which can be defined either as:

$$Q_{out} = \iint_S j_r \mathcal{H}(j_r) \, dS \tag{17}$$

or

$$Q_{in} = \iint_S j_r \mathcal{H}(-j_r)\,dS \qquad (18)$$

where S is a surface corresponding to a partition of a sphere, j_r is the radial component of the current density expressed in $A.m^{-2}$, $\mathcal{H}(j_r)$(resp. $\mathcal{H}(-j_r)$) is the Heaviside distribution equal to one if $j_r > 0$ (resp. $-j_r > 0$) and 0 if $j_r < 0$ (resp. $-j_r < 0$), and Q_{out} and Q_{in} are the total amount of current flowing respectively outward and inward of the corresponding surface S. Q_{out} and Q_{in} are expressed in Ampere, that is there are homogeneous to a current intensity. The difference with the total current intensity, however, is that only currents in one direction are accounted for in Q_{out} and Q_{in}. Note that, for the case of a poloidal currents flowing through a whole sphere, the total current intensity is strictly 0A (Sabaka et al., 2010) as currents flowing outward are compensated by currents flowing inward. The total amount of currents, however, is nonzero and reflects the quantity of currents flowing through the sphere. This quantity is therefore particularly adapted to low- and mid-latitude IHFACs which flow outward of one hemisphere and inward of the other.

6.3.1. Numerical Estimate of the Integrated Amount of IHFACs

The total amount of current Q_{out} and Q_{in} can be estimated numerically. To do so, we use the algorithm of Leopardi (2006) which allows to divide the sphere into partitions of equal area. For this study, the total sphere is divided into 1,000 partitions, which is found to provide accurate enough results. The numerical estimate of Q_{out} and Q_{in} can then be computed by, first, computing the radial current density prediction of Model A, B, or C at the center of each partition at a specific UTC and season, and, second, by computing the weighted sum of the contribution from each partition. Note that, although Q_{out} and $-Q_{in}$ must be theoretically equal—the minus sign arises because of the sign convention used in Equations 18 and 17, the numerical estimates of these two quantities might slightly differ due to numerical errors. We first check to what extent this statement is true.

Figure 12 shows a comparison between numerical estimates of Q_{out} and $-Q_{in}$ as a function of UTC, for each season, and for Model A and B. In this figure, Q_{out} and $-Q_{in}$ were computed on the dayside, defined here as the interval between 6:00 MLT and 18:00 MLT, and at low and mid latitudes, that is between ±55° of quasi dipole latitude. The rational here is to check that Q_{out} and $-Q_{in}$ are representative of low- and mid-latitude IHFACs, which mostly flow from one hemisphere to the other on the dayside. In Figure 12, we indeed observe that Q_{out} and $-Q_{in}$ are very close for all UTCs and seasons, and for both Model A and B. Additionally, the sum $Q_{out} + Q_{in}$ is represented in green. If the numerical estimates of Q_{out} and $-Q_{in}$ were perfect estimates, one should expect $Q_{out} + Q_{in}$ to be zero. We indeed observe that $Q_{out} + Q_{in}$ is close to zero, again for all UTCs and seasons, and for Model A and B. $Q_{out} + Q_{in}$ accounts at most for no more than 10% of Q_{out} and $-Q_{in}$, which is found acceptable for this study.

Although Q_{out} and $-Q_{in}$ were found to be close in Figure 12, we still observed some small differences between these two quantities. To account for these differences, we define a new quantity Q_{av}, such that:

$$Q_{av} = \frac{1}{2} \iint_S |j_r|\,dS \qquad (19)$$

which is equivalent to taking the average between Q_{out} and $-Q_{in}$. Similarly to Q_{out} and $-Q_{in}$, Q_{av} can also be computed numerically using the algorithm presented above in this section. In the following sections, Q_{av} is used to explore the dynamics of low- and mid-latitude IHFACs.

6.3.2. Total Amount of IHFACs at Low and Mid Latitudes on the Dayside

In Sections 6.1 and 6.2, IHFACs were shown to follow some significant climatological variations. In particular, it was observed that IHFACs seem to be stronger in summer and fall, although this was not properly quantified. In this section, this latter statement is discussed using the quantity Q_{av} defined in Section 6.3.1.

Figure 13 presents estimates of Q_{av} on the dayside—between 6:00 MLT and 18:00 MLT—and at low and mid latitudes—between ±55° of quasi dipole latitude—plotted as a function of UTC for both Model A and B. We first observe that low- and mid-latitude IHFACs are generally stronger in summer, which confirms what could be inferred from results in several previous studies (Lühr et al., 2015, 2019; Park, Stolle, et al., 2020; Park, Yamazaki, & Lühr, 2020). This observation, however, is quantified in terms of total amount of currents for the
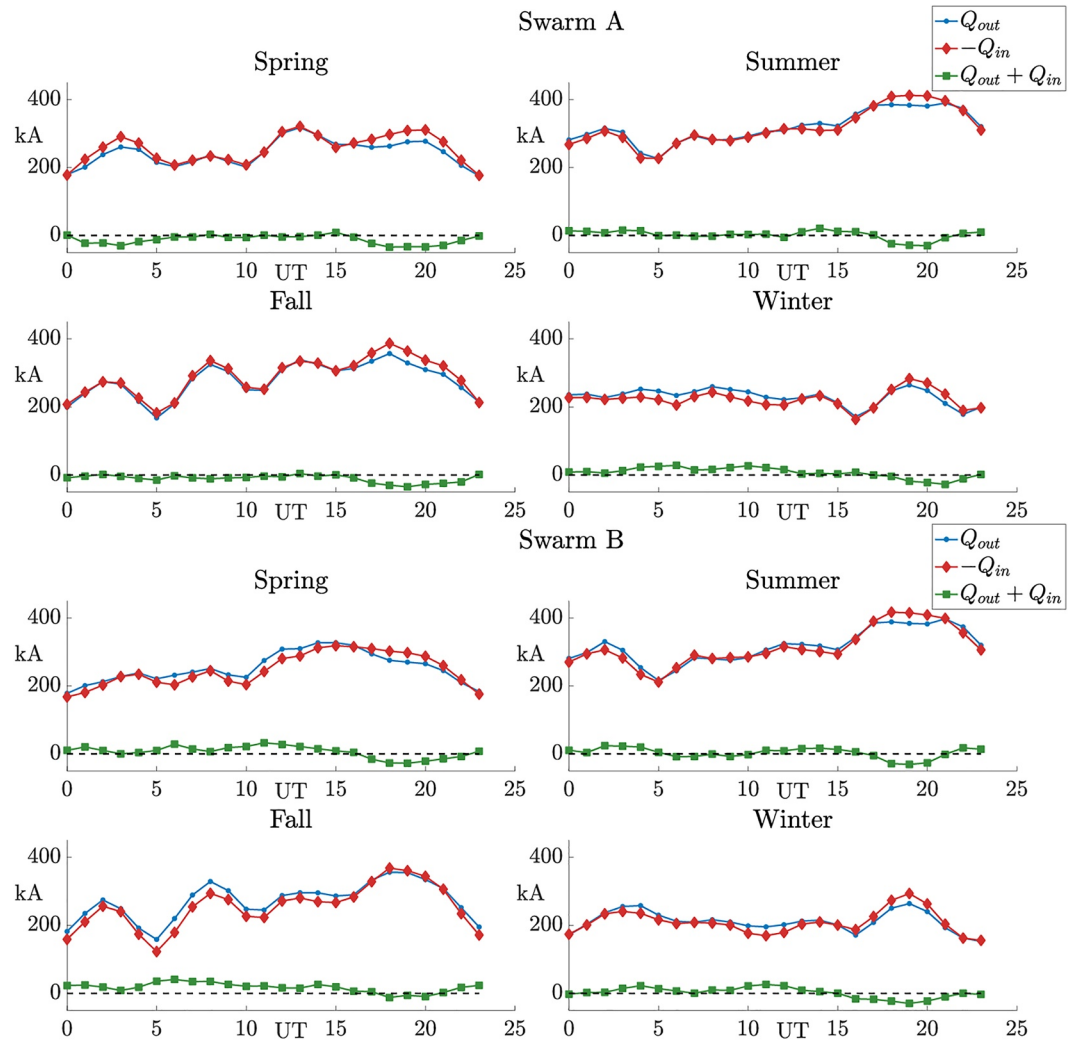
Figure 12. Comparison between Q_{out} and $-Q_{in}$ computed on the dayside (between 6:00 MLT and 18:00 MLT) and at low and mid latitudes (between $\pm 55°$ of quasi dipole latitude) as a function of UTC for Model A (upper four panels) and Model B (bottom four panels). Q_{out} is shown with blue dots, $-Q_{in}$ with red diamonds and the sum $Q_{out} + Q_{in}$ with green squares, at the spring equinox (March 20, upper left panels), summer solstice (June 20, upper right panels), fall equinox (September 22, bottom left panels) and winter solstice (December 21, bottom right panel).
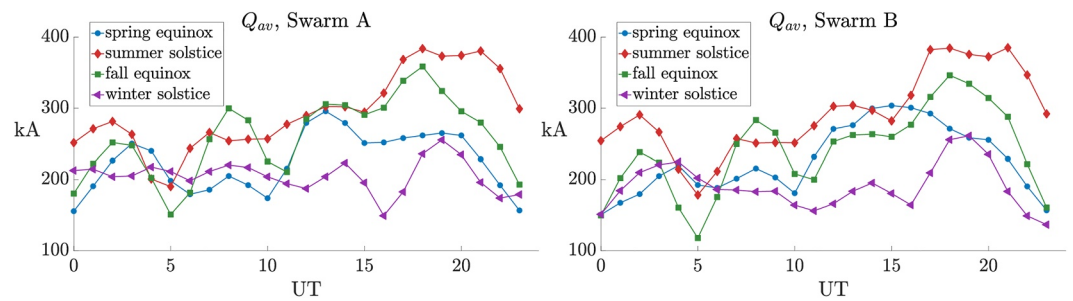

Figure 13. Q_{av} estimated on the dayside (between 6:00 MLT and 18:00 MLT) and at low and mid latitudes (between ± 55 degrees of quasi dipole latitude) as a function of UTC for Model A (left) and B (right), at the spring equinox (March 20, blue dots), summer solstice (June 20, red diamonds), spring equinox (September 22, green squares) and winter solstice (December 21, purple triangles).

first time in this study. Figure 13 also shows that the average total amount of current Q_{av} is by no means similar in fall and spring, again for both Model A and B. Indeed, Q_{av} is often stronger in fall compared to spring—although this is not systematic—and follows substantially different variations with UTC during these two seasons. Note that some significant differences between these two seasons were already observed in Sections 6.1 and 6.2.3. This confirms that IHFACs in these two seasons cannot be regarded as strictly equivalent. Additionally, Q_{av} is the weakest in winter for most UTCs.

Figure 13 also shows that the average total amount of current Q_{av} on the dayside and at low and mid latitudes is of the order of 150–350 kA for all UTCs and seasons—as could also be observed in Figure 12. Interestingly, these values are of the same order of magnitude than the currents predicted with E-region equivalent current functions, which can be computed using either physics-based models (Yamazaki et al., 2016; Yamazaki & Maute, 2017) or empirical models derived with ground and satellite magnetic data (Chulliat et al., 2013, 2016; C. Owolabi et al., 2021; Yamazaki, 2022; Yamazaki et al., 2011). Note, however, that a comparison between Q_{av} and currents predicted with these equivalent functions is not straightforward, as the first represents the integrated current crossing a partition of a sphere in the F region whereas the second is usually represented as bands of horizontal currents in the E region. Nevertheless, this highlights that the F-region current system is not negligible compared to the E-region current system. This consideration is particularly important as recent studies have discussed potential contamination of IHFACs in external field models of the ionospheric E-region Sq currents, in particular in relation with their cross-equatorial part (Yamazaki, 2022).

One can also observe in Figure 13 that Q_{av} is generally stronger between 16:00 UTC and 22:00 UTC. This is particularly marked in summer and fall, whereas it is less significant in spring and winter. At these UTCs, the dayside is over the SSA region and the Pacific Ocean. The reason for this increase is still unclear, although some elements of discussion are presented in Section 6.3.3. Finally, the longitudinal modulation of IHFACs can be discerned, mostly on the curves corresponding to summer and fall. Note, however, that IHFACs at low latitudes and at mid latitudes are known to follow different variations with longitude (Park, Yamazaki, & Lühr, 2020, and Section 6.1 of this paper). The variations of IHFACs in these two latitude sectors are not separated in Figure 13 because Q_{av} is computed between $\pm 55°$ of quasi dipole latitude. Therefore, a discussion of IHFAC modulation with longitude in Figure 13 is not very relevant.

6.3.3. IHFAC Longitudinal Modulation at Low Latitudes

IHFACs are driven by the asymmetric action of the E-region ionospheric dynamo about the magnetic equator—which results from an hemispheric asymmetry of neutral winds and conductivity—(Richmond, 1989; Chulliat et al., 2005, and references therein). In particular, the key role played by solar upward propagating nonmigrating tides for IHFAC longitudinal modulation has been highlighted in several studies (Lühr et al., 2019; Park et al., 2011; Park, Yamazaki, & Lühr, 2020). These tides are excited in the troposphere, propagate upward and reach their maximum amplitude in the mesosphere lower thermosphere region—roughly between 80 and 120 km—(Forbes et al., 2008; Hagan & Forbes, 2002), which largely overlaps the E-region ionosphere. At these altitudes, they are thought to influence the ionospheric dynamo (Liu, 2016; Yiğit et al., 2016; Yiğit & Medvedev, 2015). These tides can be produced by the release of latent heat from tropical clouds, land-sea contrasts and non-linear interactions between tides and planetary waves (Forbes, 2021; Hagan et al., 2007; Oberheide et al., 2015; Oberheide & Forbes, 2008; Schindelegger et al., 2023). The different modes are referred to using a 3-character code, each character specifying—in this order—the period, the direction of propagation and the wavenumber (Forbes, 2021). The letters D and S refer to diurnal and semi-diurnal modes, whereas the letters W and E refer to westward and eastward propagating modes. An important mode is the DE3, standing for a wavenumber-3 eastward propagating mode. Nonmigrating tides are by definition non Sun-synchronous, as opposed to migrating tides that migrate with the apparent motion of the Sun. Note that nonmigrating tides are also well-known to drive a significant part of the longitudinal variations of the equatorial electrojet (Lühr et al., 2008; Soares et al., 2018, 2022) as well as to influence the F-region ionospheric plasma density (England, 2012; Immel et al., 2006; Schindelegger et al., 2023).

Figure 14 presents estimates of Q_{av} at low magnetic latitudes—between $\pm 35°$ of quasi dipole latitude—and in 1-hr MLT bands as a function of UTC and MLT. In Figure 14, Q_{av} was computed using the model predictions on 20 March 2016 (spring equinox, first row), 20 June 2016 (summer solstice, second row), 22 September 2016 (fall equinox, third row), and 21 December 2016 (winter solstice, fourth row). The panels in the left column correspond to Model A whereas the panels in the right column correspond to Model B (see also Figure S6 in Supporting Information S1 for Model C). The values of Q_{av} are shown on a logarithmic color scale to accentuate the day-night contrast. Figure 14 shows that almost all the low-latitude IHFACs predicted by the model flow
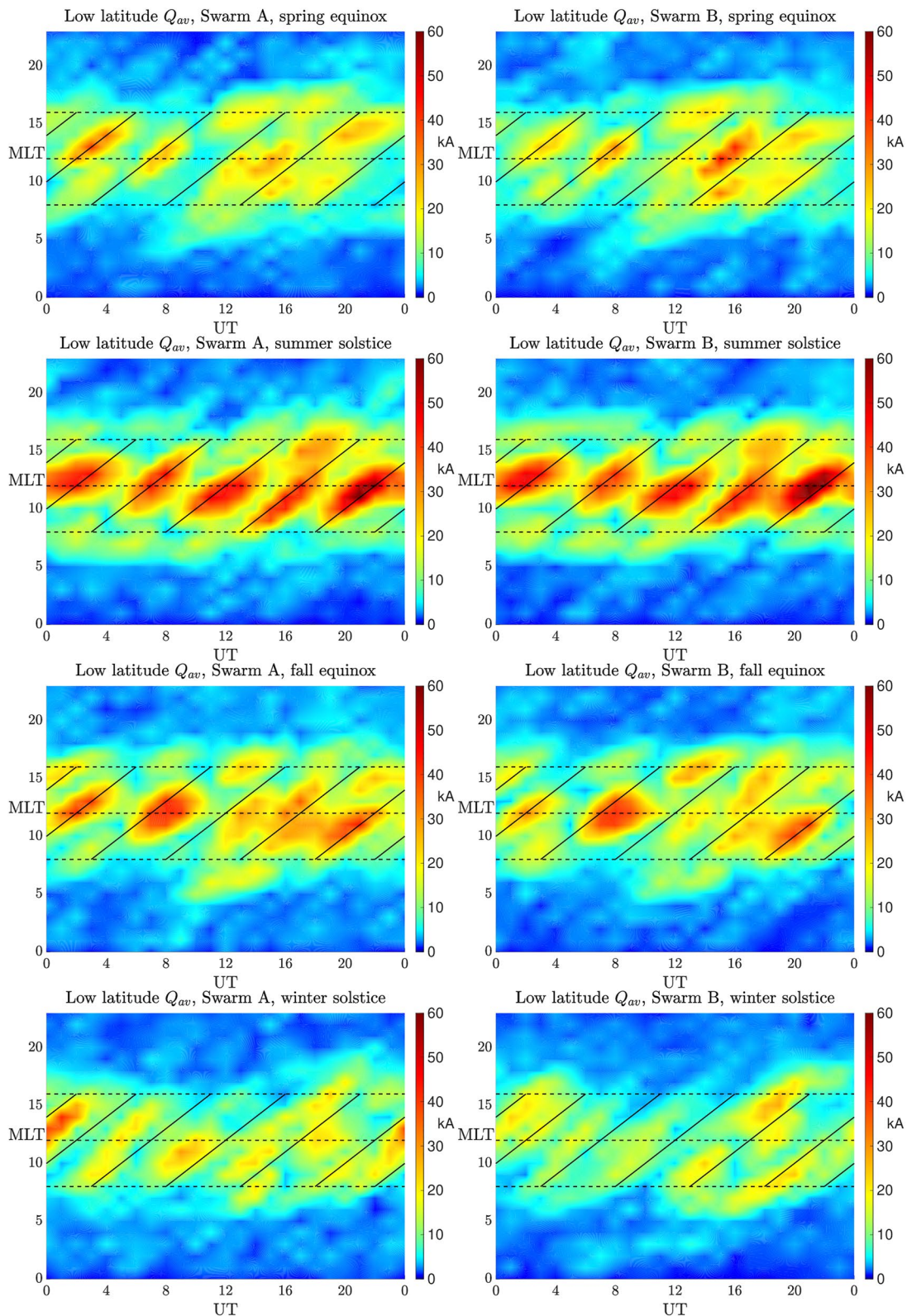
Figure 14. Q_{av} estimated in 1 hour MLT bands and at low latitudes (between ± 35 degrees of quasi dipole latitude) as a function of UTC and MLT, at the spring equinox (March 20, first row), summer solstice (June 20, second row), fall equinox (September 22, third row) and winter solstice (December 21, fourth row), and for Model A (left) and B (right). The values of Q_{av} are represented with a logarithmic color scale. The three horizontal dashed lines mark a MLT of 8:00 (bottom), noon (center) and 16:00 (upper). Five transversal black plain lines with a slope of 1 MLT.UTC^{-1} are shown at regular intervals of 5:00 UTC.

on the dayside between 06:00 MLT and 17:00 MLT, for both Model A and B. Furthermore, the longitudinal modulation of low-latitude IHFACs can be clearly observed in this figure—here shown as a function of UTC. In summer—second row, we observe a clear WN-5 structure, confirming what was suggested by Park, Yamazaki, and Lühr (2020) and what can be observed in Figure 8e of Park, Stolle, et al. (2020). However, the WN-5 structure is not as clearly visible in Spring, Fall, and Winter. This longitudinal modulation varies significantly with season and seems to be an important factor controlling the overall magnitude of low-latitude IHFACs. But most strikingly, the IHFAC structures are not aligned with lines of fixed MLT—dashed black lines in Figure 14, but rather with the transversal black plain lines with a slope of 1 MLT.UTC^{-1}. This observation shows that, in a reference frame fixed with respect to the Sun, low-latitude IHFACs mostly drift eastward at the same speed as the rotation of the Earth. There is, however, one obvious exception. Indeed, in the panels corresponding to summer—second row, the IHFAC eastward drift is slowed at about 0:00 UTC and the observed structure is more aligned with the horizontal dashed line marking 12:00 MLT. This eastward drifting behavior is also clearly seen in the movies we provide in Supporting Information S1, where low-latitude IHFACs in summer clearly arise in the morning sector and next drift eastward before vanishing in the evening sector.

The results shown in Figure 14 provide some constraints on the driving mechanism producing the observed longitudinal modulation of low-latitude IHFACs. The eastward drift of IHFACs strongly supports that the longitudinal modulation is driven by a physical process co-rotating with the Earth, potentially being the action on the E-region dynamo of upward propagating nonmigrating tides originating from the troposphere. The DE3 mode, produced by the release of latent heat in the troposphere (Hagan & Forbes, 2002; Miyoshi et al., 2017; Oberheide & Forbes, 2008), is thought to play an important part (Lühr et al., 2019; Park, Yamazaki, & Lühr, 2020). This mode produces a WN-4 structure in the F-region ionosphere (Wan et al., 2012), however, in summer the IHFACs are closer to a WN-5 structure according to Figure 14. This suggests that DE3 alone might not be sufficient to explain the full longitudinal variability of IHFACs and that other modes, such as the DE4 mode, might also be important. Additionally, the increase of total amount of currents over the Pacific Ocean in summer observed in Section 6.3.2 might also be an important consideration potentially highlighting the importance of land-sea contrasts. Nonmigrating tides are also known to follow some significant variations with season, and in particular the DE3 mode which is enhanced in summer (Oberheide et al., 2011; Sridharan, 2019). This might contribute to explain the seasonal variability observed in Figure 14. The complex relationship between upward propagating nonmigrating tides and low-latitude IHFACs will need to be further explored.

7. Conclusion

We derived a new climatological model designed to represent the toroidal magnetic fields and the associated radial poloidal currents at low and mid latitudes at the altitude of the Swarm satellites. This model consists of three independent spherical harmonics representations—respectively, labeled Model A, B, and C, each computed with the data of one Swarm satellite. The parametrization relies on the Mie representation of the magnetic field in a thin shell and a truncated spherical harmonics expansion in geographic spherical coordinates, modulated by harmonic functions of time representing several annual and diurnal modes. The model reproduces well the average climatological signal in the magnetic data for all three Swarm satellites. Additionally, it predicts realistic low- and mid-latitude radial F-region currents generally in agreement with results obtained in previous studies. These currents are mostly antisymmetric with respect to the magnetic equator which is a clear signature of low- and mid-latitude IHFACs.

The model was used to analyze the climatology of low- and mid-latitude IHFACs. It was confirmed that low- and mid-latitude IHFACs can change polarity with latitude, although these changes of polarity are often confined to specific local time sectors. Low- and mid-latitude IHFACs also follow some significant variations with longitude at all seasons. In particular, the geometry of the main field was shown to be an important factor controlling these variations. A longitudinal modulation of these currents was also observed, most significant in Summer, Spring, and Fall, confirming observations from previous studies. Furthermore, a clear picture of IHFAC average daily variations in winter was provided. Although some clear morphological differences exist between summer and winter, low- and mid-latitude IHFACs often flow in the same direction during these two seasons. Low- and mid-latitude IHFACs indeed follow a more complex climatology than the one described by Fukushima's conceptual model. Some clear differences between IHFACs in fall and spring could also be identified.

The model predictions were further analyzed using numerical estimates of the total amount of current, an integrated quantity that represents the quantity of current flowing from one hemisphere to the other along the field

lines. The main result is the identification of the eastward drift of IHFACs at the same speed as the rotation of the Earth. This eastward drift will need to be confirmed using the Level-2 FAC Swarm product (Ritter et al., 2013), although some limitations could arise due to known uncertainties in this product (Fillion et al., 2021; F. Wang, Lühr, et al., 2022). Other characteristics such as the increase of total amount of current over the Pacific Ocean—particularly significant in summer—or the occurrence of a WN-5 longitudinal structure in summer are also important. In the future, the relationship between these characteristics and upward propagating nonmigrating tides should be investigated more thoroughly as these tides could exert a strong control on low- and mid-latitude IHFACs.

The model also includes high-latitude data, although the currents predicted at these latitudes were not discussed. High-latitude F-region currents are very dynamic and the climatological parametrization used in this study cannot account for these dynamics. One should be aware that the high-latitude signal could be affected by temporal aliasing of fast-varying high-latitude magnetic fields. More work is needed to develop a model including F-region currents at all latitudes.

Data Availability Statement

The Swarm satellite data used in this study are available from ESA at http://swarm-diss.eo.esa.int/. The software to compute the toroidal magnetic field and radial poloidal current density from the model coefficients can be downloaded at https://doi.org/10.18715/IPGP.2023.lddfo4so.

References

Abidin, Z. Z., Jusoh, M., Abbas, M., Bolaji, O., & Yoshikawa, A. (2019). Features of the inter-hemispheric field-aligned current system over Malaysia ionosphere. *Journal of Atmospheric and Solar-Terrestrial Physics*, *192*, 104769. https://doi.org/10.1016/j.jastp.2018.01.012

Alken, P., Maute, A., Richmond, A. D., Vanhamäki, H., & Egbert, G. D. (2017). An application of principal component analysis to the interpretation of ionospheric current systems: Tiegcm modeling, PCA, and data fitting. *Journal of Geophysical Research: Space Physics*, *122*(5), 5687–5708. https://doi.org/10.1002/2017ja024051

Amm, O., Vanhamäki, H., Kauristie, K., Stolle, C., Christiansen, F., Haagmans, R., et al. (2015). A method to derive maps of ionospheric conductances, currents, and convection from the Swarm multisatellite mission. *Journal of Geophysical Research: Space Physics*, *120*(4), 3263–3282. https://doi.org/10.1002/2014ja020154

Amm, O., & Viljanen, A. (1999). Ionospheric disturbance magnetic field continuation from the ground to the ionosphere using spherical elementary current systems. *Earth Planets and Space*, *51*(6), 431–440. https://doi.org/10.1186/bf03352247

Backus, G. (1986). Poloidal and toroidal fields in geomagnetic field modeling. *Reviews of Geophysics*, *24*(1), 75. https://doi.org/10.1029/rg024i001p00075

Baerenzung, J., Holschneider, M., Wicht, J., Lesur, V., & Sanchez, S. (2020). The Kalmag model as a candidate for IGRF-13. *Earth Planets and Space*, *72*(1). (Number: 1 Publisher: Published for the Society of Geomagnetism and Earth, Planetary, and Space Sciences (SGEPSS), the Seismological Society of Japan, the Volcanological Society of Japan, the Geodetic Society of Japan, the Japanese Society for Planetary Sciences by Terra Scien). https://doi.org/10.1186/s40623-020-01295-y

Bolaji, O., Rabiu, A., Oyeyemi, E., & Yumoto, K. (2012). Climatology of the inter-hemispheric field-aligned currents system over the Nigeria ionosphere. *Journal of Atmospheric and Solar-Terrestrial Physics*, *89*, 144–153. https://doi.org/10.1016/j.jastp.2012.07.008

Chulliat, A., Blanter, E., Le Mouël, J.-L., & Shnirman, M. (2005). On the seasonal asymmetry of the diurnal and semidiurnal geomagnetic variations. *Journal of Geophysical Research*, *110*(A5), A05301. https://doi.org/10.1029/2004ja010551

Chulliat, A., Vigneron, P., & Hulot, G. (2016). First results from the swarm Dedicated ionospheric field inversion chain. *Earth Planets and Space*, *68*(1), 104. https://doi.org/10.1186/s40623-016-0481-6

Chulliat, A., Vigneron, P., Thébault, E., Sirol, O., & Hulot, G. (2013). Swarm SCARF dedicated ionospheric field inversion chain. *Earth Planets and Space*, *65*(11), 1271–1283. https://doi.org/10.5047/eps.2013.08.006

Egbert, G. D., Alken, P., Maute, A., & Zhang, H. (2021). Modelling diurnal variation magnetic fields due to ionospheric currents. *Geophysical Journal International*, *225*(2), 1086–1109. https://doi.org/10.1093/gji/ggaa533

England, S. L. (2012). A review of the effects of non-migrating atmospheric tides on the Earth's low-latitude ionosphere. *Space Science Reviews*, *168*(1), 211–236. https://doi.org/10.1007/s11214-011-9842-4

Fathy, A., Ghamry, E., & Arora, K. (2019). Mid and low-latitudinal ionospheric field-aligned currents derived from the Swarm satellite constellation and their variations with local time, longitude, and season. *Advances in Space Research*, *64*(8), 1600–1614. https://doi.org/10.1016/j.asr.2019.07.022

Fillion, M., Hulot, G., Alken, P., Chulliat, A., & Vigneron, P. (2021). Multispacecraft current density estimates in the low- and mid-latitude F-region ionosphere using the swarm constellation. *Journal of Geophysical Research: Space Physics*, *126*(7), e2020JA028872. https://doi.org/10.1029/2020ja028872

Finlay, C. C., Lesur, V., Thébault, E., Vervelidou, F., Morschhauser, A., & Shore, R. (2017). Challenges handling magnetospheric and ionospheric signals in internal geomagnetic field modelling. *Space Science Reviews*, *206*(1–4), 157–189. https://doi.org/10.1007/s11214-016-0285-9

Forbes, J. M. (2021). Atmosphere-ionosphere (A-I) coupling by solar and lunar tides. In *Upper atmosphere dynamics and energetics* (pp. 157–181). American Geophysical Union (AGU). https://doi.org/10.1002/9781119815631.ch9

Forbes, J. M., Zhang, X., Palo, S., Russell, J., Mertens, C. J., & Mlynczak, M. (2008). Tidal variability in the ionospheric dynamo region. *Journal of Geophysical Research*, *113*(A2). https://doi.org/10.1029/2007ja012737

Friis-Christensen, E., Lühr, H., & Hulot, G. (2006). Swarm: A constellation to study the Earth's magnetic field. *Earth Planets and Space*, *58*(4), 351–358. https://doi.org/10.1186/bf03351933

Fukushima, N. (1978). Electric potential difference between conjugate points in middle latitudes caused by asymmetric dynamo in the iono-spheret (Vol. *9*).

Fukushima, N. (1994). Some topics and historical episodes in geomagnetism and aeronomy. *Journal of Geophysical Research*, *99*(A10), 19113. https://doi.org/10.1029/94ja00102

Hagan, M. E., & Forbes, J. M. (2002). Migrating and nonmigrating diurnal tides in the middle and upper atmosphere excited by tropospheric latent heat release. *Journal of Geophysical Research*, *107*(D24), ACL61–ACL615. https://doi.org/10.1029/2001jd001236

Hagan, M. E., Maute, A., Roble, R. G., Richmond, A. D., Immel, T. J., & England, S. L. (2007). Connections between deep tropical clouds and the Earth's ionosphere. *Geophysical Research Letters*, *34*(20), L20109. https://doi.org/10.1029/2007gl030142

Holschneider, M., Lesur, V., Mauerberger, S., & Baerenzung, J. (2016). Correlation-based modeling and separation of geomagnetic field compo-nents: Correlation-based modeling. *Journal of Geophysical Research: Solid Earth*, *121*(5), 3142–3160. https://doi.org/10.1002/2015jb012629

Hulot, G., Sabaka, T., Olsen, N., & Fournier, A. (2015). The present and future geomagnetic field. In *Treatise on geophysics* (pp. 33–78). Elsevier. https://doi.org/10.1016/b978-0-444-53802-4.00096-8

Immel, T. J., Sagawa, E., England, S. L., Henderson, S. B., Hagan, M. E., Mende, S. B., et al. (2006). Control of equatorial ionospheric morphol-ogy by atmospheric tides. *Geophysical Research Letters*, *33*(15), L15108. https://doi.org/10.1029/2006gl026161

Laundal, K. M., Finlay, C. C., & Olsen, N. (2016). Sunlight effects on the 3D polar current system determined from low Earth orbit measure-ments. *Earth Planets and Space*, *68*(1), 142. https://doi.org/10.1186/s40623-016-0518-x

Laundal, K. M., Finlay, C. C., Olsen, N., & Reistad, J. P. (2018). Solar wind and seasonal influence on ionospheric currents from swarm and CHAMP measurements. *Journal of Geophysical Research: Space Physics*, *123*(5), 4402–4429. https://doi.org/10.1029/2018ja025387

Léger, J.-M., Jager, T., Bertrand, F., Hulot, G., Brocco, L., Vigneron, P., et al. (2015). In-flight performance of the Absolute Scalar Magnetometer vector mode on board the Swarm satellites. *Earth Planets and Space*, *67*(1), 57. https://doi.org/10.1186/s40623-015-0231-1

Leopardi, P. (2006). A partition of the unit sphere into regions of equal area and small diameter. *Electronic Transactions on Numerical Analysis*, *25*(12), 309–327.

Le Sager, P., & Huang, T. S. (2002). Ionospheric currents and field-aligned currents generated by dynamo action in an asymmetric Earth magnetic field. *Journal of Geophysical Research*, *107*(A2), SIA4-1–SIA4-14. https://doi.org/10.1029/2001ja000211

Liu, H.-L. (2016). Variability and predictability of the space environment as related to lower atmosphere forcing. *Space Weather*, *14*(9), 634–658. https://doi.org/10.1002/2016sw001450

Loan, C. F. V. (2000). The ubiquitous Kronecker product. *Journal of Computational and Applied Mathematics*, *123*(1), 85–100. https://doi.org/10.1016/s0377-0427(00)00393-9

Lühr, H., Alken, P., & Zhou, Y.-L. (2021). The equatorial electrojet. In *Ionosphere dynamics and applications* (pp. 281–299). American Geophys-ical Union (AGU). https://doi.org/10.1002/9781119815617.ch12

Lühr, H., Kervalishvili, G., Michaelis, I., Rauberg, J., Ritter, P., Park, J., et al. (2015). The interhemispheric and F region dynamo currents revis-ited with the Swarm constellation: Lühr et al., Midlatitude FACs from Swarm. *Geophysical Research Letters*, *42*(9), 3069–3075. https://doi.org/10.1002/2015gl063662

Lühr, H., Kervalishvili, G. N., Stolle, C., Rauberg, J., & Michaelis, I. (2019). Average characteristics of low-latitude interhemispheric and F region dynamo currents deduced from the swarm satellite constellation. *Journal of Geophysical Research: Space Physics*, *124*(12), 10631–10644. https://doi.org/10.1029/2019ja027419

Lühr, H., & Maus, S. (2006). Direct observation of the F region dynamo currents and the spatial structure of the EEJ by CHAMP. *Geophysical Research Letters*, *33*(24), L24102. https://doi.org/10.1029/2006gl028374

Lühr, H., Rother, M., Häusler, K., Alken, P., & Maus, S. (2008). The influence of nonmigrating tides on the longitudinal variation of the equatorial electrojet. *Journal of Geophysical Research*, *113*(A8). https://doi.org/10.1029/2008ja013064

Matsushita, S. (1968). Sq and L current systems in the ionosphere. *Geophysical Journal of the Royal Astronomical Society*, *15*(1–2), 109–125. https://doi.org/10.1111/j.1365-246X.1968.tb05751.x

Matzka, J., Stolle, C., Yamazaki, Y., Bronkalla, O., & Morschhauser, A. (2021). The geomagnetic Kp index and derived indices of geomagnetic activity. *Space Weather*, *19*(5). https://doi.org/10.1029/2020sw002641

Maute, A., & Richmond, A. D. (2017). F-region dynamo simulations at low and mid-latitude. *Space Science Reviews*, *206*(1–4), 471–493. https://doi.org/10.1007/s11214-016-0262-3

Merayo, J. M., Jørgensen, J. L., Friis-Christensen, E., Brauer, P., Primdahl, F., Jørgensen, P. S., et al. (2008). The swarm magnetometry package: IAA: 6th symposium on small satellites for Earth observation. *Small Satellites for Earth Observation*, 143–151.

Miyoshi, Y., Pancheva, D., Mukhtarov, P., Jin, H., Fujiwara, H., & Shinagawa, H. (2017). Excitation mechanism of non-migrating tides. *Journal of Atmospheric and Solar-Terrestrial Physics*, *156*, 24–36. https://doi.org/10.1016/j.jastp.2017.02.012

Oberheide, J., & Forbes, J. M. (2008). Tidal propagation of deep tropical cloud signatures into the thermosphere from TIMED observations. *Geophysical Research Letters*, *35*(4), L04816. https://doi.org/10.1029/2007gl032397

Oberheide, J., Forbes, J. M., Zhang, X., & Bruinsma, S. L. (2011). Climatology of upward propagating diurnal and semidiurnal tides in the ther-mosphere. *Journal of Geophysical Research*, *116*(A11). https://doi.org/10.1029/2011ja016784

Oberheide, J., Hagan, M. E., Richmond, A. D., & Forbes, J. M. (2015). Dynamical meteorology | atmospheric tides. In G. R. North, J. Pyle, & F. Zhang (Eds.), *Encyclopedia of atmospheric sciences* (2nd ed., pp. 287–297). Academic Press. https://doi.org/10.1016/b978-0-12-382225-3.00409-6

Olsen, N. (1997). Ionospheric F region currents at middle and low latitudes estimated from Magsat data. *Journal of Geophysical Research*, *102*(A3), 4563–4576. https://doi.org/10.1029/96ja02949

Olsen, N., Friis-Christensen, E., Floberghagen, R., Alken, P., Beggan, C. D., Chulliat, A., et al. (2013). The swarm satellite constellation appli-cation and research Facility (SCARF) and swarm data products. *Earth Planets and Space*, *65*(11), 1189–1200. https://doi.org/10.5047/eps.2013.07.001

Owolabi, C., Ruan, H., Yamazaki, Y., Li, J., Zhong, J., Eyelade, A. V., et al. (2021). Empirical modeling of ionospheric current using empirical Orthogonal function analysis and artificial neural network. *Space Weather*, *19*(11), e2021SW002831. https://doi.org/10.1029/2021sw002831

Owolabi, O. P., Bolaji, O. S., Adeniyi, J. O., Oyeyemi, E. O., Rabiu, A. B., & Habarulema, J. B. (2018). Excursions of interhemispheric field-aligned currents in Africa. *Journal of Geophysical Research: Space Physics*, *123*(7), 6042–6053. https://doi.org/10.1029/2017ja025083

Park, J., Lühr, H., & Min, K. W. (2010). Characteristics of F -region dynamo currents deduced from CHAMP magnetic field measurements: F-region dynamo currents. *Journal of Geophysical Research*, *115*(A10). https://doi.org/10.1029/2010ja015604

Park, J., Lühr, H., & Min, K. W. (2011). Climatology of the inter-hemispheric field-aligned current system in the equatorial ionosphere as observed by CHAMP. *Annales Geophysicae*, *29*(3), 573–582. https://doi.org/10.5194/angeo-29-573-2011

Park, J., Stolle, C., Yamazaki, Y., Rauberg, J., Michaelis, I., & Olsen, N. (2020). Diagnosing low-/mid-latitude ionospheric currents using plat-form magnetometers: CryoSat-2 and GRACE-FO. *Earth Planets and Space*, *72*(1), 162. https://doi.org/10.1186/s40623-020-01274-3

Park, J., Yamazaki, Y., & Lühr, H. (2020). Latitude dependence of interhemispheric field-aligned currents (IHFACs) as observed by the swarm constellation. *Journal of Geophysical Research: Space Physics*, *125*(2). https://doi.org/10.1029/2019ja027694

Ranasinghe, M., Fujimoto, A., Yoshikawa, A., & Jayaratne, C. (2021). Seasonal variation of inter-hemispheric field-aligned currents deduced from time-series analysis of the equatorial geomagnetic field data during solar cycle 23–24. *Earth Planets and Space*, *73*(1), 146. https://doi.org/10.1186/s40623-021-01481-6

Richmond, A. D. (1979). Ionospheric wind dynamo theory: A review. *Journal of Geomagnetism and Geoelectricity*, *31*(3), 287–310. https://doi.org/10.5636/jgg.31.287

Richmond, A. D. (1989). Modeling the ionosphere wind dynamo: A review. *Pure and Applied Geophysics*, *131*(3), 413–435. https://doi.org/10.1007/BF00876837

Richmond, A. D. (1995). Ionospheric electrodynamics using magnetic apex coordinates. *Journal of Geomagnetism and Geoelectricity*, *47*(2), 191–212. https://doi.org/10.5636/jgg.47.191

Rishbeth, H. (1971). The F-layer dynamo. *Planetary and Space Science*, *19*(2), 263–267. https://doi.org/10.1016/0032-0633(71)90205-4

Rishbeth, H. (1981). The F-region dynamo. *Journal of Atmospheric and Terrestrial Physics*, *43*(5), 387–392. https://doi.org/10.1016/0021-9169(81)90102-1

Rishbeth, H. (1997). The ionospheric E-layer and F-layer dynamos—A tutorial review. *Journal of Atmospheric and Solar-Terrestrial Physics*, *59*(15), 1873–1880. https://doi.org/10.1016/s1364-6826(97)00005-9

Ritter, P., Lühr, H., & Rauberg, J. (2013). Determining field-aligned currents with the Swarm constellation mission. *Earth Planets and Space*, *65*(11), 1285–1294. https://doi.org/10.5047/eps.2013.09.006

Sabaka, T. J., Hulot, G., & Olsen, N. (2010). Mathematical properties relevant to geomagnetic field modeling. In W. Freeden, M. Zuhair Nashed, & T. Sonar (Eds.), *Handbook of geomathematics* (pp. 1–37). Springer. https://doi.org/10.1007/978-3-642-27793-1_17-2

Sabaka, T. J., & Olsen, N. (2006). Enhancing comprehensive inversions using the Swarm constellation. *Earth Planets and Space*, *58*(4), 371–395. https://doi.org/10.1186/bf03351935

Sabaka, T. J., Olsen, N., & Langel, R. A. (2002). A comprehensive model of the quiet-time, near-Earth magnetic field: Phase 3. *Geophysical Journal International*, *151*(1), 32–68. https://doi.org/10.1046/j.1365-246x.2002.01774.x

Sabaka, T. J., Olsen, N., Tyler, R. H., & Kuvshinov, A. (2015). CM5, a pre-Swarm comprehensive geomagnetic field model derived from over 12 yr of CHAMP, Ørsted, SAC-C and observatory data. *Geophysical Journal International*, *200*(3), 1596–1626. https://doi.org/10.1093/gji/ggu493

Sabaka, T. J., Tøffner-Clausen, L., Olsen, N., & Finlay, C. C. (2018). A comprehensive model of Earth's magnetic field determined from 4 years of Swarm satellite observations. *Earth Planets and Space*, *70*(1), 130. https://doi.org/10.1186/s40623-018-0896-3

Sabaka, T. J., Tøffner-Clausen, L., Olsen, N., & Finlay, C. C. (2020). CM6: A comprehensive geomagnetic field model derived from both CHAMP and swarm satellite observations. *Earth Planets and Space*, *72*(1), 80. https://doi.org/10.1186/s40623-020-01210-5

Schindelegger, M., Sakazaki, T., & Green, M. (2023). Chapter 16 - Atmospheric tides—An Earth system signal. In M. Green & J. C. Duarte (Eds.), *A journey through tides* (pp. 389–416). Elsevier. https://doi.org/10.1016/b978-0-323-90851-1.00007-8

Shinbori, A., Koyama, Y., Nosé, M., Hori, T., & Otsuka, Y. (2017). Characteristics of seasonal variation and solar activity dependence of the geomagnetic solar quiet daily variation. *Journal of Geophysical Research: Space Physics*, *122*(10), 10796–10810. https://doi.org/10.1002/2017ja024342

Soares, G., Yamazaki, Y., Matzka, J., Pinheiro, K., Morschhauser, A., Stolle, C., & Alken, P. (2018). Equatorial counter electrojet longitudinal and seasonal variability in the American sector. *Journal of Geophysical Research: Space Physics*, *123*(11), 9906–9920. https://doi.org/10.1029/2018ja025968

Soares, G., Yamazaki, Y., Morschhauser, A., Matzka, J., Pinheiro, K. J., Stolle, C., et al. (2022). Using principal component analysis of satellite and ground magnetic data to model the equatorial electrojet and derive its tidal composition. *Journal of Geophysical Research: Space Physics*, *127*(9), e2022JA030691. https://doi.org/10.1029/2022ja030691

Sridharan, S. (2019). Seasonal variations of low-latitude migrating and nonmigrating diurnal and semidiurnal tides in timed-saber temperature and their relationship with source variations. *Journal of Geophysical Research: Space Physics*, *124*(5), 3558–3572. https://doi.org/10.1029/2018ja026190

Takeda, M. (1982). Three dimensional ionospheric currents and field aligned currents generated by asymmetrical dynamo action in the ionosphere. *Journal of Atmospheric and Terrestrial Physics*, *44*(2), 187–193. https://doi.org/10.1016/0021-9169(82)90122-2

Van Sabben, D. (1966). Magnetospheric currents, associated with the N-S asymmetry of Sq. *Journal of Atmospheric and Terrestrial Physics*, *28*(10), 965–982. https://doi.org/10.1016/s0021-9169(17)30026-0

Wan, W., Ren, Z., Ding, F., Xiong, J., Liu, L., Ning, B., et al. (2012). A simulation study for the couplings between DE3 tide and longitudinal WN4 structure in the thermosphere and ionosphere. *Journal of Atmospheric and Solar-Terrestrial Physics*, *90–91*, 52–60. https://doi.org/10.1016/j.jastp.2012.04.011

Wang, F., Lühr, H., Xiong, C., & Zhou, Y. (2022). Improved field-aligned current and radial current estimates at low and middle latitudes deduced by the swarm dual-spacecraft. *Journal of Geophysical Research: Space Physics*, *127*(6), e2022JA030396. https://doi.org/10.1029/2022ja030396

Wang, H., Xia, H., Zhang, K., Zhong, Y., & Qian, C. (2022). Local time and longitudinal variation of the ionospheric radial current: Swarm observations and TIE–GCM simulations. *Earth Planets and Space*, *74*(1), 151. https://doi.org/10.1186/s40623-022-01714-2

Weimer, D. R., Clauer, C. R., Engebretson, M. J., Hansen, T. L., Gleisner, H., Mann, I., & Yumoto, K. (2010). Statistical maps of geomagnetic perturbations as a function of the interplanetary magnetic field. *Journal of Geophysical Research*, *115*(A10). https://doi.org/10.1029/2010ja015540

Winch, D. E., Ivers, D. J., Turner, J. P. R., & Stening, R. J. (2005). Geomagnetism and Schmidt quasi-normalization. *Geophysical Journal International*, *160*(2), 487–504. https://doi.org/10.1111/j.1365-246x.2004.02472.x

Yamashita, S. (2002). Seasonal and local time dependences of the interhemispheric field-aligned currents deduced from the Ørsted satellite and the ground geomagnetic observations. *Journal of Geophysical Research*, *107*(A11), 1372. https://doi.org/10.1029/2002ja009414

Yamazaki, Y. (2022). Solar and lunar daily geomagnetic variations and their equivalent current systems observed by Swarm. *Earth Planets and Space*, *74*(1), 99. https://doi.org/10.1186/s40623-022-01656-9

Yamazaki, Y., Häusler, K., & Wild, J. A. (2016). Day-to-day variability of midlatitude ionospheric currents due to magnetospheric and lower atmospheric forcing. *Journal of Geophysical Research: Space Physics*, *121*(7), 7067–7086. https://doi.org/10.1002/2016ja022817

Yamazaki, Y., & Maute, A. (2017). Sq and EEJ—A review on the daily variation of the geomagnetic field caused by ionospheric dynamo currents. *Space Science Reviews*, *206*(1–4), 299–405. https://doi.org/10.1007/s11214-016-0282-z

Yamazaki, Y., Yumoto, K., Cardinal, M. G., Fraser, B. J., Hattori, P., Kakinami, Y., et al. (2011). An empirical model of the quiet daily geomagnetic field variation: Empirical SQ field model. *Journal of Geophysical Research*, *116*(A10). https://doi.org/10.1029/2011ja016487

Yiğit, E., Koucká Knížová, P., Georgieva, K., & Ward, W. (2016). A review of vertical coupling in the Atmosphere–Ionosphere system: Effects of waves, sudden stratospheric warmings, space weather, and of solar activity. *Journal of Atmospheric and Solar-Terrestrial Physics*, *141*, 1–12. https://doi.org/10.1016/j.jastp.2016.02.011

Yiğit, E., & Medvedev, A. S. (2015). Internal wave coupling processes in Earth's atmosphere. *Advances in Space Research*, *55*(4), 983–1003. https://doi.org/10.1016/j.asr.2014.11.020